Friedrich-Alexander-Universität
Naturwissenschaftliche Fakultät

Master's Thesis
in Physics

Improving the reconstruction of gamma-ray events in HESS telescope using an asymmetric Gaussian fitting method

Geethika Konduru

Supervisor: Prof. Dr. Stefan Funk

Erlangen Centre for Astroparticle Physics

Submission date: 24-06-25

Abstract

The High Energy Stereoscopic System (H.E.S.S.) detectors detect gamma-ray events by capturing the Cherenkov light emitted from extensive air shower particles as elliptical images in its camera plane. Conventionally, these images are characterized using Hillas parameters, the geometric moments that describe the shape, orientation, and intensity distribution of the shower to perform energy and angular reconstruction. In this work, we present an alternative method of characterization and reconstruction based on fitting an asymmetric two-dimensional Gaussian function to the shower images. This model provides parameters such as the centroid, major and minor axes, amplitude, direction, and skewness of the shower image. Using simulated gamma-ray showers, we compare the performance of our asymmetric Gaussian fitting approach with the standard Hillas-based parametrization.

Contents

1 Introduction

The universe presents itself to us through two distinct faces: one governed by thermal processes, the other by extreme relativistic phenomena. On the one hand, we observe the familiar thermal universe, from the cosmic microwave background to starlight and accretion disk emission, which dominates the observable sky and informs much of our astrophysical understanding. Yet coexisting with this thermal realm is a more enigmatic, high-energy universe, where particles are accelerated to extraordinary energies through processes that we cannot recreate in terrestrial laboratories. This non-thermal universe manifests most conspicuously through cosmic rays, whose origins remain uncertain despite nearly a century of study, though likely born in the shock waves of supernova explosions. These particles, some carrying energies millions of times greater than what our most powerful particle accelerators can produce, follow a characteristic power-law distribution that immediately distinguishes them from thermal sources. While thermal emission reveals the universe in equilibrium, these relativistic processes illuminate the most violent and energetic phenomena in nature.

In the late 19th century, scientists using gold-leaf electroscopes noticed unexplained slow discharges in gases, even when isolated from known radiation sources. In 1901, Elster and Geitel in Germany and C.T.R. Wilson in England independently concluded that this was caused by unknown ionizing radiation, with Wilson speculating that it might originate beyond Earth's atmosphere. The breakthrough came in 1907 when Theodore Wulf invented a portable electroscope to measure radiation at different altitudes[excerpt from *McDonald and Ptuskin, 2001*]. Contrary to the expectations of this radiation to decrease at higher altitudes (based on the assumption that the source is terrestrial), measurements proved otherwise. Intrigued by this phenomenon, an Austrian nuclear physicist, Victor Hess, conducted a series of balloon flights on 12 August 1912. In his paper, Hess[*Hess, 1912*] determined that these findings were most likely caused by highly penetrating radiation entering Earth's atmosphere from space, which produced ionization even in ground-level instruments. This radiation was later named 'cosmic rays' by Robert Millikan[*Millikan and Cameron, 1928*].

Cosmic rays are high-velocity charged particles consisting of 90% protons, 9% heavy nuclei, and 1% electrons. Their elemental and isotopic composition offers insight into their origins, acceleration mechanisms, and propagation through interstellar space. A complete understanding of cosmic-ray acceleration and transport through the interstellar medium is essential for refining cosmological models. In recent years, gamma-ray and neutrino astronomy have become powerful observational tools for investigating cosmic ray properties. Unlike charged particles(cosmic rays), these neutral messengers propagate undeflected by galactic or extragalactic magnetic fields, thereby preserving directional information about their acceleration sites. Consequently, the detection of these particles may provide an indirect means of identifying cosmic-ray sources and probing the physical

processes occurring within particle acceleration regions. Neutrinos possess exceptionally small weak interaction cross sections[*Di Sciascio, 2019*], enabling them to escape dense astrophysical environments. This unique property allows neutrinos to carry direct information from the interiors and immediate vicinities of compact cosmic sources such as supernovae and active galactic nuclei(AGN). However, the fundamental experimental challenge involves achieving statistically significant separation between neutrino-induced muon signals and the overwhelming background of atmospheric muons produced by hadronic showers from primary cosmic rays.

The high-energy universe reveals its nature through non-thermal gamma-ray emission, which escapes the obscuring thermal foreground radiation that dominates lower energies. While relativistic processes like AGN jets require multiwavelength observations to fully constrain particle acceleration mechanisms, gamma-ray emission provides critical insights into the highest-energy processes. This makes gamma-ray astronomy essential for probing extreme astrophysical environments inaccessible to other wavebands. The main objective of high-energy gamma-ray astronomy is to identify and study various emission sources, ranging from compact objects to diffuse structures. Additionally, this field enables exploration of extreme astrophysical processes and contributes to cosmological and particle physics research.

Gamma rays form the highest-energy portion of the electromagnetic spectrum. By astronomical convention, photons with energies above 100keV are classified as gamma rays. Measurements by the LHAASO collaboration in 2021 have extended the known gamma-ray energy range to petaelectronvolt (PeV) scales [*Cao et al., 2021*], demonstrating that this spectral band spans at least ten orders of magnitude (from 10^5 eV to 10^{15}eV). This extraordinary breadth makes the gamma-ray domain both the widest in the electromagnetic spectrum and the most diverse in terms of physical characteristics. Gamma-ray astronomy began with Explorer XI's first detections[*Kraushaar et al., 1965*], but significant progress came with SAS-2 (1972–73), which collected 8000 photons (30MeV–5GeV; *Fichtel et al., 1975*). Imaging Atmospheric Cherenkov Telescopes (IACTs) have proven to be one of the most successful instruments in the history of Very High Energy (VHE) gamma-ray astronomy. Among these, the High Energy Stereoscopic System (H.E.S.S.) array stands out as a premier facility, having detected more than 70 VHE gamma-ray sources to date. Located in Namibia, H.E.S.S. utilizes an array of large optical telescopes to detect the faint Cherenkov radiation emitted by extensive air showers produced when gamma rays interact with Earth's atmosphere.

This thesis examines the traditional analysis techniques used to reconstruct gamma-ray air showers from H.E.S.S. observations, which rely heavily on parameterizations of the Cherenkov light distribution. Building on these established methods, an improved analysis approach is proposed that enhances statistical significance. This new technique aims to improve energy and angular resolution through better shower profile characterization.

2 Production of γ rays

The acceleration of charged particles(cosmic rays) to relativistic energies also leads to the production of gamma rays via non-thermal processes, such as inverse Compton scattering, bremsstrahlung, and pion decay. Since gamma-rays propagate unimpeded by galactic and extragalactic magnetic fields due to their neutral charge, their trajectories retain the directional information from their source. Consequently, the detection and spectral analysis of very high-energy (VHE) gamma-rays serve as a direct probe for identifying cosmic-ray acceleration sites. This method enables the study of extreme astrophysical environments such as supernova remnants, active galactic nuclei, and gamma-ray bursts, where particle acceleration mechanisms operate under non-thermal conditions. In the past twenty years, very high-energy (VHE) gamma-ray astronomy has undergone significant advancements, marked by the detection of over two hundred sources spanning different astrophysical classes and categories. This chapter aims to discuss different mechanisms for VHE gamma-ray emission in astronomical environments and gives a brief overview of detected sources.

VHE gamma-ray emission arises from either leptonic (inverse Compton, synchrotron) or hadronic (pion decay) processes, driven by particle acceleration to ultra-relativistic energies. Possible mechanisms for cosmic-ray particle acceleration are:

- **Second order Fermi acceleration:** Proposed by Enrico Fermi in 1949[*Fermi, 1949*, this mechanism describes the gradual energization of charged particles through repeated collisions with magnetized plasma clouds or turbulent structures in the interstellar medium (ISM). These clouds, linked to irregularities in Galactic magnetic fields, act as scattering centers.

- **First order Fermi acceleration:** Also known as diffusive shock acceleration, this mechanism involves the efficient acceleration of charged particles at collisionless shock waves. Unlike stochastic (second-order) processes, it relies on systematic energy gain per shock crossing, making it a dominant mechanism for producing cosmic rays up to ultra-high energies ($\sim$ PeV).

- **Magnetic reconnection:** This process occurs when oppositely directed magnetic field lines in a highly conductive plasma undergo topological rearrangement through breaking and subsequent reconnection. The reconfiguration of magnetic field topology results in efficient conversion of stored magnetic energy into kinetic energy of plasma flows, thermal heating, and non-thermal particle acceleration to high energies.

The following section examines the dominant VHE gamma-ray production mechanisms, organized by their physical origin: leptonic processes and hadronic processes.

2.1 Leptonic Processes

2.1.1 Inverse Compton scattering

The quantum phenomenon of Compton scattering describes how photons undergo wavelength shifts when interacting with electrons due to relativistic effects. When a photon scatters off a stationary electron, its wavelength changes following the relation:

$$\frac{\Delta\lambda}{\lambda} = \left(\frac{\hbar\omega}{m_e c^2}\right)(1 - \cos\alpha) \tag{2.1}$$

where α represents the photon's deflection angle. It is evident from this equation that the energy of the scattered photon cannot be larger than the energy of the incident photon. However, when low-energy photons collide with extremely fast-moving electrons, the photons can gain energy through inverse Compton (IC) scattering, a process in which the electron's kinetic energy is effectively transferred to the photon. This mechanism becomes particularly significant in high-energy astrophysics, where it becomes a gamma-ray production channel in environments containing both dense photon fields and high-energy electrons like Active Galactic Nuclei(AGN) jets, Pulsar wind nebulae etc.

2.1.2 Synchroton radiation

Synchrotron radiation serves as the primary mechanism for high-energy photon production in magnetized astrophysical environments. The trajectories of relativistic charged particles are governed by Lorentz forces exerted by ambient magnetic fields, causing them to follow curved paths. As these accelerated particles spiral through magnetic field lines, they emit characteristic synchrotron radiation across a broad spectrum, typically peaking in the X-ray to gamma-ray range for ultra-relativistic electrons. For an electron population following a power-law energy distribution $N(E) \propto E^{-p}$, where p is the power law index and E is the energy of the electron, the resulting synchrotron photon spectrum takes the form:

$$\phi_\gamma(E_\gamma) \propto E_\gamma^{-(p+1)/2} \tag{2.2}$$

where E_γ is the energy of the photon after scattering.

This fundamental process dominates the initial phase of high-energy emission in numerous cosmic sources, including pulsar wind nebulae, active galactic nuclei jets, and supernova remnants, where strong magnetic fields and particle acceleration coexist.

2.1.3 Relativistic Bremsstrahlung

The process in which a charged particle is accelerated in the Coulomb field of another charged particle to emit electromagnetic radiation is called Bremsstrahlung

or free-free emission. From classical electrodynamics, the ion's Coulomb field transforms into a short, intense pulse of nearly transverse electromagnetic radiation. For the stationary electron, this pulse resembles an incoming photon beam. The electron then scatters this radiation via the Compton process, generating the final observed gamma-ray emission. Assuming that the electrons follow a similar power law as in the previous case, the emmitted radiation spectrum is given as

$$\phi_\gamma(E_\gamma) \propto E_\gamma^{-p} \tag{2.3}$$

A visual representation of the discussed gamma-ray production mechanisms is shown in Figure 2.1

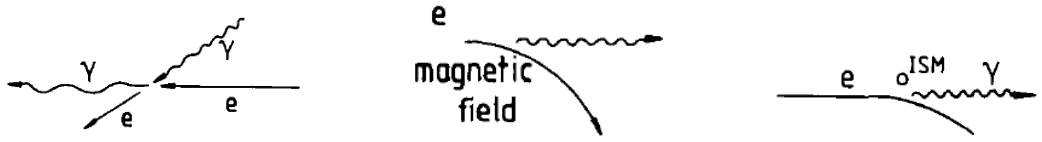

(a) (b) (c)

Figure 2.1: Schematic of leptonic gamma ray production mechanisms (a) Inverse Compton scattering, (b) Synchrotron radiation, and (c) relativistic Bremsstrahlung[*Murthy and Wolfendale, 1993*]

Figure 2.2 illustrates how high-energy electrons evolve over time and the radiation they produce in the Galactic center region. The light gray curve shows the initial power-law energy distribution of injected electrons (spectral index $\alpha = 2$), where energy is equally distributed across logarithmic scales. As these electrons age (here, over 1,000 years), they lose energy through synchrotron radiation and inverse Compton scattering, causing the spectrum to steepen (dashed dark gray line). A distinct "cooling break" appears near 1.2TeV, beyond which the electron spectrum drops more sharply due to accelerated energy loss at higher energies. The resulting radiation, synchrotron (peaking in X-rays) and inverse Compton (peaking in gamma-rays), is shown in orange, with the IC spectrum suppressed above $\sim$ 10TeV due to Klein-Nishina effects, where scattering becomes inefficient. A weaker magnetic field (3μG, light gray curve) shifts the cooling break higher and reduces synchrotron emission, demonstrating how environmental conditions alter spectral features.

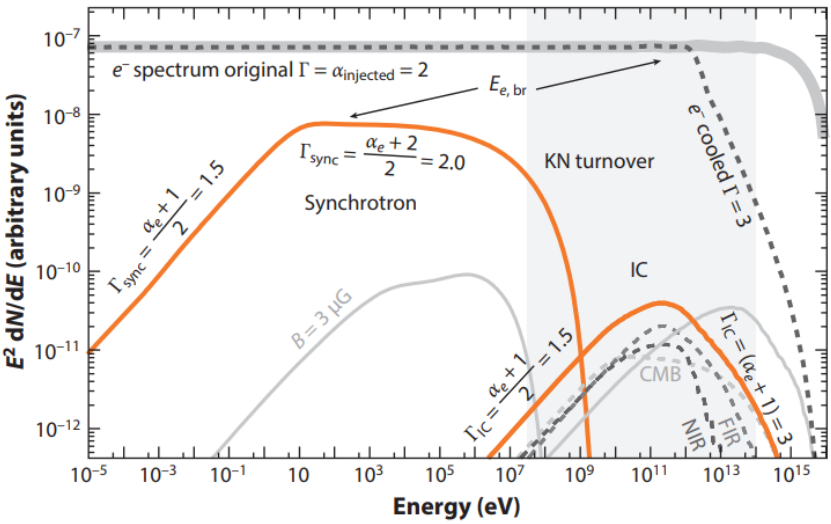

Figure 2.2: A spectral energy distribution showcasing the electron spectrum depicted in light gray alongside the emitted Synchrotron and Inverse Compton radiation depicted in orange[*Funk, 2015*]

2.2 Hadronic Processes

High-energy protons can, in principle, produce gamma rays just like electrons through processes like Bremsstrahlung, but protons are far less efficient because of their large mass. Protons mainly rely on strong force interactions with matter or radiation, producing unstable particles(mesons) that decay into gamma rays. When protons interact with other protons or matter, they produce neutral and charged pions in almost equal numbers. The charged pions decay into muons and neutrinos, while the neutral pions decay into two gamma-ray photons. Secondary pions maintain the spectral shape of their parent protons. It is believed that cosmic rays are accelerated through first-order Fermi processes (yielding $p \approx 2$ spectra), the resulting hadronic gamma-rays should correspondingly display E^{-2} spectra. The correlated production of neutral and charged pions in these interactions implies that neutrino observations would provide definitive proof of cosmic-ray acceleration environments.

The figure 2.3 shows how high-energy protons interact with interstellar matter to produce gamma rays and secondary particles. The gray curve in the top right represents the initial proton spectrum, a power law with index $\alpha = 2.0$ that cuts off sharply at 100TeV. At lower energies (below $\sim$ 500MeV), the gamma-ray spectrum turns over due to fundamental physics of pion decay: there's a minimum energy needed to create these particles, causing the dramatic drop below 67.5MeV. The plot also shows secondary electrons/positrons (dashed gray curve) made when charged pions decay, which then emit synchrotron radiation peaking at $1 - 10$eV as they spiral through the galaxy's 30μG magnetic field. The shaded area marks

where current gamma-ray telescopes like Fermi-LAT operate, allowing scientists to compare these predictions with real observations.

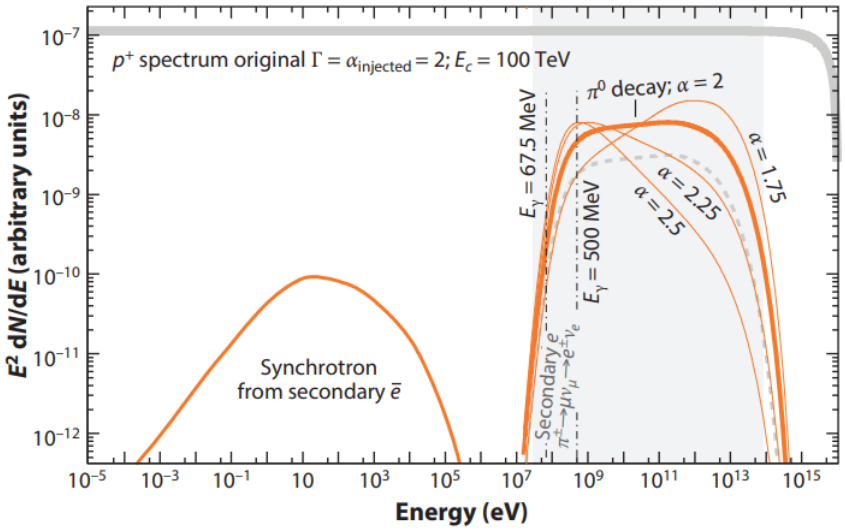

Figure 2.3: A spectral energy distribution showcasing the hadron(proton) spectrum depicted in light gray alongside the emitted gamma radiation due to Pion decay depicted in orange[*Funk, 2015*]

2.3 Sources of VHE γ rays

The Crab Nebula marked a pivotal milestone in the study of VHE gamma-ray astronomy when it became the first source detected with high statistical significance by the Whipple imaging atmospheric Cherenkov telescope (IACT) in 1989[*Weekes et al., 1989*]. However, progress in the field was initially slow; by the year 2000, only eight VHE gamma-ray sources had been identified. This changed drastically after 2005, thanks to significant advancements in IACT sensitivity. Today, over 240 VHE gamma-ray sources have been detected, a remarkable increase attributed to the development of stereoscopic IACT arrays such as H.E.S.S., MAGIC, and VERITAS. These modern telescopes can detect the Crab Nebula at a 5σ significance level in just minutes, a task that required 25 hours of observation during the Whipple era. The upcoming Cherenkov Telescope Array Observatory(CTAO) is expected to revolutionize the field further, improving sensitivity by an order of magnitude and enabling the detection of the Crab Nebula in under a minute. By the end of the decade, the number of known VHE sources is projected to reach around a thousand, vastly expanding our understanding of the high-energy universe. An illustration of known VHE gamma-ray sources is shown in Figure 2.4.

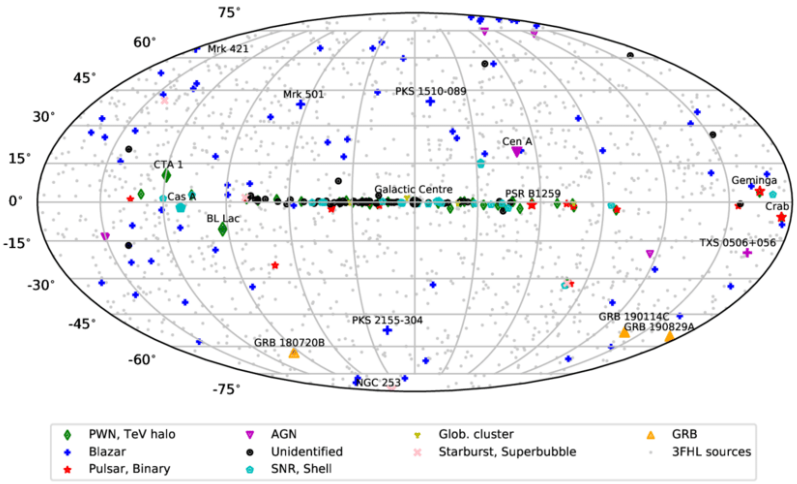

Figure 2.4: The TeV sky as of mid-2019, showcasing a compilation of known VHE gamma-ray sources from TeVCat alongside high-energy sources from the Fermi-LAT 3FHL catalog[*Hinton and Ruiz-Velasco, 2020*]

VHE gamma rays originate from a diverse range of astrophysical sources, both within and beyond our galaxy. Galactic sources include supernova remnants (SNRs), pulsar wind nebulae (PWNe), and pulsars, which are among the most prominent emitters of VHE radiation. Extragalactic sources, on the other hand, include AGN, whose relativistic jets produce intense gamma-ray emission, as well as starburst galaxies (SBGs) and gamma-ray bursts (GRBs), which exhibit transient but extremely energetic afterglows. Despite these discoveries, a significant number of VHE sources remain unidentified, particularly along the galactic plane, necessitating further multi-wavelength observations to determine their nature. The continued expansion of VHE gamma-ray astronomy promises to uncover new classes of high-energy phenomena, deepening our knowledge of particle acceleration and extreme astrophysical environments.

3 Detection of γ rays

Gamma rays interact with matter through different physical processes depending on their energy. At lower energies, they are primarily absorbed via the photoelectric effect, while at medium energies, Compton scattering dominates. At the highest energies (above 1 MeV), pair production becomes the main interaction mechanism. Because of these fundamental differences, astronomers must use specialized detection techniques tailored to specific energy ranges, from scintillation detectors and Compton telescopes at MeV energies to atmospheric Cherenkov telescopes for TeV gamma rays. This chapter examines how gamma-ray interactions with matter vary across different energy levels. It then presents an overview of modern detection techniques, focusing specifically on the instrumentation and methodologies most relevant for the energy ranges discussed in this paper.

3.1 Photon interactions

Gamma rays interact with matter through three primary mechanisms, each dominating at different energy ranges. At low energies (typically below $\sim$ 500keV), the **Photoelectric Effect** prevails, where an incident photon transfers all its energy to a bound electron, ejecting it from the atom. The probability of this interaction scales strongly with atomic number (Z). This explains why dense, high-Z materials like lead or cadmium are commonly used in gamma-ray shielding and detection.

At intermediate energies ($\sim$ 500keV $-$ 5MeV), **Compton scattering** becomes dominant. Here, the photon scatters off a loosely bound or free electron, transferring only part of its energy and changing direction. Unlike the photoelectric effect, Compton scattering depends less on atomic number and more on electron density. In thick materials, a photon may undergo multiple Compton scatterings before eventually being absorbed via the photoelectric effect. At even higher energies ($>$ 1.022MeV), **Pair Production** takes over, where the photon converts into an electron-positron pair in the presence of a nucleus. This process requires a minimum photon energy of twice the electron rest mass (1.022MeV) and becomes increasingly probable at higher energies. The relative importance of these interactions varies with photon energy, as illustrated in Figure 3.1

As mentioned above, gamma rays cover energies from keV to PeV, a range so vast that no single detector can measure them all efficiently. The detection process involves detecting numerous gamma-ray photons while precisely measuring their arrival time, direction, and energy with the highest possible resolution in terms of timing, spatial accuracy, and energy. This means that a huge section of the sky needs to be monitored 24/7. An ideal detector would excel in sensitivity, angular and energy resolution, while also covering a wide portion of the sky and operating almost continuously without downtime. However, no single detector can perfectly achieve all these capabilities simultaneously. For example, instruments

with wide fields of view generally have worse angular or energy resolution. To address the detection challenges posed by gamma rays across different energy ranges, astronomers employ specialized instrumentation tailored to each energy band, as conventional optical methods are ineffective due to the highly penetrating nature of these photons. The detection efficiency is fundamentally governed by the physical interaction cross-sections between gamma rays and detector materials, necessitating distinct technological approaches: scintillation crystals or semiconductor trackers for $\mathrm{MeV} - \mathrm{GeV}$ energies, and extensive atmospheric Cherenkov telescope arrays for TeV energies. Consequently, the geometric dimensions and material composition of the detector systems become the primary determinants of both effective collection area and angular resolution, making the detector's physical scale and design critical factors in observational capability. This energy-dependent detection paradigm requires optimizing trade-offs between sensitivity, field of view, and energy resolution for each specific scientific application.

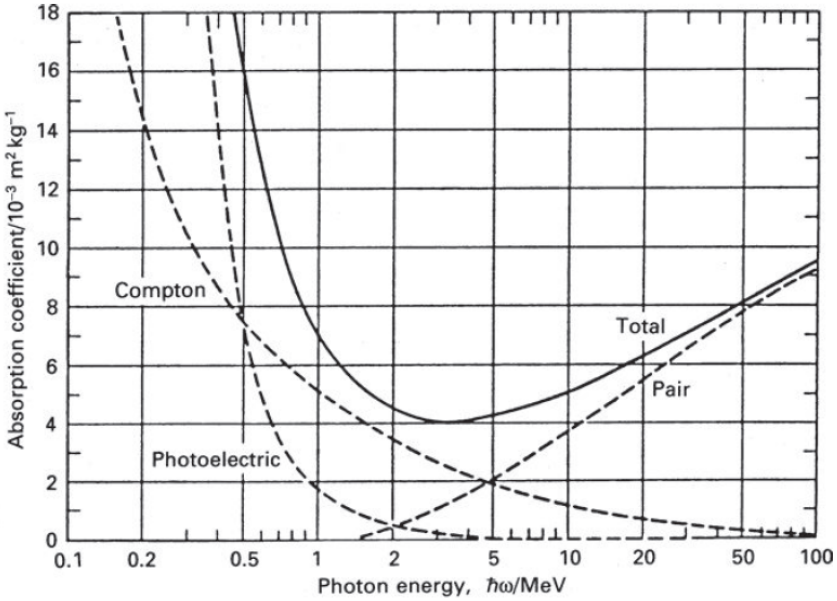

Figure 3.1: The mass absorption coefficient of high-energy photons in lead, showing the relative contributions from three dominant interaction processes: photoelectric absorption, Compton scattering, and electron-positron pair production[*Longair, 2011*]

Gamma-ray detectors are broadly classified into two categories based on their deployment: space-based and ground-based telescopes. Space telescopes, such as Fermi-LAT, operate under strict size and weight limitations, restricting their effective energy range to $\leq 100\mathrm{GeV}$. However, they offer two key advantages: (1) significantly low background interference since there are no atmospheric particles, and (2) a wide field of view, enabling all-sky monitoring. Conversely, ground-based instruments like Cherenkov telescopes must contend with substantial atmospheric

background noise and narrower fields of view. Yet their massive detection areas ($\geq 10,000$ m^2) make them uniquely capable of detecting ultra-high-energy gamma rays from 100GeV up to several PeV through extensive air shower observations. The advantages and challenges of these approaches will be explored in detail through the various detectors and detection techniques discussed in the following sections, mainly focusing on the relevant detector for this paper.

3.2 Space Telescopes

Direct detection of γ rays requires a space-based telescope since most of them are blocked or absorbed by the Earth's atmosphere.

Low-energy gamma-rays ($<$ 10MeV) are detected using either scintillation detectors or semiconductor detectors, both converting photon energy into quantifiable electronic signals. Scintillation detectors are a class of instruments that convert high-energy radiation (e.g., gamma rays) into detectable optical or near-visible light. These detectors utilize materials, typically inorganic crystals such as thallium-doped sodium iodide (NaI(Tl)) or bismuth germanate (BGO), that emit light when excited by ionizing radiation. When a high-energy photon interacts with the scintillator, it produces a flash of light that is then amplified and recorded by photomultiplier tubes (PMTs) or silicon photomultipliers (SiPMs). The key advantages of scintillators include their nanosecond-scale response time, and they can be divided into small, precise sections to better track where radiation hits. Due to their fast timing and large field of view, scintillation detectors are particularly well-suited for detecting fast transients, such as gamma-ray bursts (GRBs). Historically, they were among the first technologies used in gamma-ray astronomy. Some notable examples are: BATSE(Burst and Transient Source Experiment) onboard the Compton Gamma-Ray Observatory(CGRO), which used eight NaI(Tl) detectors covering the full sky to provide rapid burst triggers and GBM (Gamma-ray Burst Monitor) on Fermi, which combines twelve NaI detectors (sensitive from 8 keV to 1 MeV) and two BGO detectors (150 keV–30 MeV)[*Prandini et al., 2023*] to achieve broad spectral coverage and a near-all-sky field of view (9.5 steradians). Upon detecting a transient, GBM rapidly calculates preliminary positions to enable follow-up observations by other instruments, such as Fermi's Large Area Telescope (LAT).

Compton telescopes are used for detecting gamma rays in the MeV energy range, where Compton scattering dominates photon interactions. These instruments employ a two-stage detection system: an initial scattering detector (typically a low-Z material) measures the photon's recoil angle and energy loss, while a second absorption detector (often a high-Z calorimeter) captures the remaining energy, enabling reconstruction of the incident photon's properties. One example is COMPTEL aboard the Compton Gamma-Ray Observatory (CGRO), which used a liquid scintillator for scattering and NaI crystals for absorption, surrounded by plastic scintillator anticoincidence shields to reject charged-particle

background[*Schönfelder et al., 1993*]. Future missions like e-ASTROGAM plan to operate in the energy ranges of 0.3 MeV–3 GeV with two orders of magnitude improved sensitivity over COMPTEL and added polarization measurement capabilities [*De Angelis et al., 2018*], advancing multi-messenger studies of extreme astrophysical phenomena.

In the energy range of 100MeV to 100GeV, gamma-ray telescopes primarily rely on pair production. As discussed before, this interaction becomes more efficient with higher atomic number (Z) materials, which is why detectors incorporate dense metals like tungsten or lead as conversion layers. Once the pairs are created, their paths are tracked through precision detectors (such as silicon strips or spark chambers), while their energy is measured by a scintillating calorimeter. By analyzing the trajectories and energy deposits of these particles, astronomers can reconstruct the original gamma ray's direction and energy with high accuracy. A major evolution in this field began with NASA's EGRET (1991–2000), which used a spark chamber for tracking and a NaIf calorimeter, achieving the first all-sky survey in this energy range[*Thompson et al., 1993*]. The real breakthrough came with Fermi-LAT (launched in 2008), which introduced silicon strip detectors for superior tracking, along with a segmented CsI calorimeter and a plastic scintillator anticoincidence system to reject cosmic-ray background[*Atwood et al., 2009*]. Fermi-LAT's design has set the standard for modern GeV gamma-ray astronomy, providing over a decade of high-precision data. Future missions aim to further improve sensitivity and angular resolution, building on Fermi's legacy.

3.3 Ground-based Telescopes

In the Very High Energy (VHE) range (typically gamma rays above 100 GeV), astrophysical sources exhibit extremely low photon fluxes and steep spectral energy distributions. The detection of these faint and rare signals requires detectors with large effective areas. Due to these size requirements, space-based telescopes become impractical, necessitating the use of ground-based observation systems for VHE gamma-ray astronomy. However, Earth's atmosphere effectively shields against these gamma rays through interactions with atmospheric nuclei, making direct detection impossible. Consequently, only secondary effects of this atmospheric absorption can be observed, requiring the properties of the primary gamma rays to be reconstructed from measurements of the resulting secondary particles.

When high-energy gamma rays interact with matter, they primarily undergo pair production, creating electron-positron pairs. These relativistic charged particles then generate secondary gamma rays via bremsstrahlung radiation, initiating an electromagnetic cascade that propagates through the atmosphere and the resulting shower has on average, a maximum at 10km altitude. Each charged particle in this shower exceeding the Cherenkov threshold velocity ($v > c/n$, where n is the atmospheric refractive index) emits characteristic blue Cherenkov radiation. The emission occurs at a characteristic angle θ. Notably, as the refractive index

increases with decreasing altitude, the Cherenkov angle widens from approximately 0.66° at 10 km altitude to 0.74° at 8 km. There are two primary methods for ground-based VHE astronomy(represented in Figure 3.2):

- **Water Cherenkov Detectors(WCDs)** located at high altitudes measure the charged particles of the air shower.
- **Imaging Atmospheric Cherenkov Telescopes(IACTs)** located at moderate altitudes collect the Cherenkov light emitted by charged particles.

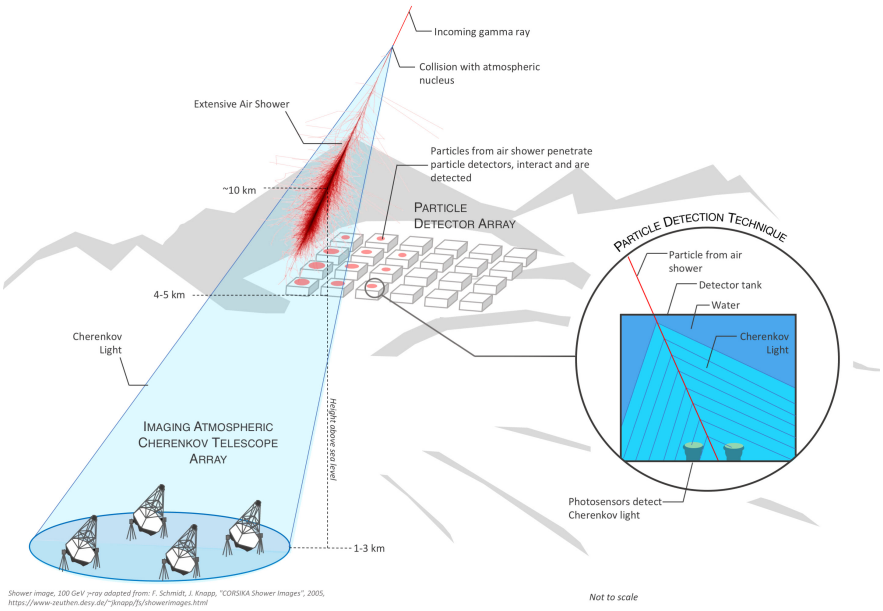

Figure 3.2: Schematic illustration of gamma-ray propagation through Earth's atmosphere, depicting the resulting electromagnetic cascade and the two ground-based detection methods at different altitudes[*SWGO Collaboration, 2023*]

The next sections provide an overview of WCD detectors and IACTs, with a focused analysis of the High Energy Stereoscopic System (H.E.S.S.), the key instrument for this paper.

3.3.1 EAS

When a high-energy gamma-ray photon penetrates Earth's atmosphere, it primarily engages in electromagnetic processes. The initial interaction typically involves pair production, whereby the gamma ray converts into an electron-positron pair. These relativistic charged particles then emit bremsstrahlung radiation as they decelerate in the atmospheric medium, producing secondary gamma rays of substantial energy. This electromagnetic cascade perpetuates through successive generations of pair production and bremsstrahlung, effectively multiplying the

number of particles while progressively diminishing their energies, this is visualized in Figure 3.3a. The cascade reaches its peak development when the average energy per particle approaches the critical energy threshold of approximately 84MeV, at which point the particle population within the air shower attains its maximum. The atmospheric altitude corresponding to this state of maximum particle multiplicity is termed the shower maximum. Beyond this point, as the shower propagates deeper into the atmosphere, energy dissipation occurs predominantly through ionization losses rather than the creation of additional particles, as shown in Figure 3.3b. Consequently, the number of particles within the air shower gradually diminishes with increasing atmospheric depth, marking the decay phase of the cascade.

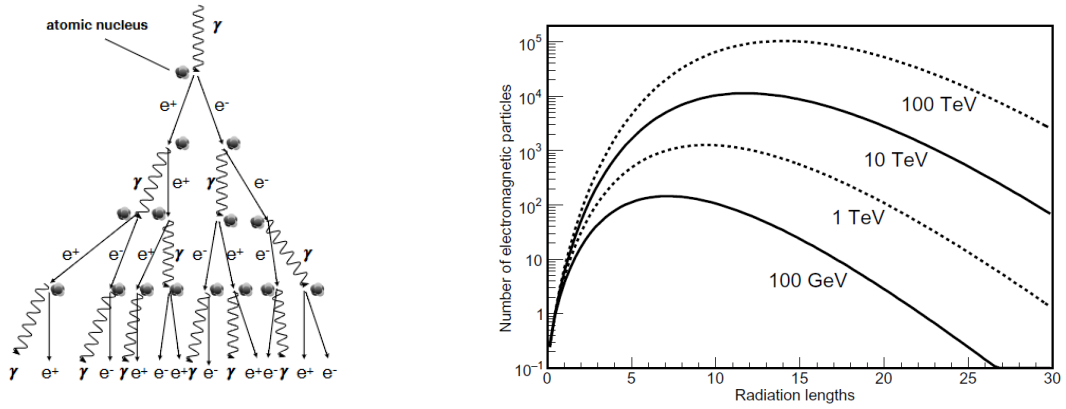

(a) (b)

Figure 3.3: (a) Schematic of an air shower development[*Steppa, 2022*], (b) Longitudinal development of an EAS shower simulated for various primary gamma-ray energies. The x-axis shows atmospheric depth in radiation lengths(Key atmospheric depths include sea level (28 radiation lengths), 2600 m (20), 4300 m (16.5), and 5200 m (14.7).)[*Sinnis, 2009*]

Not only high-energy gamma rays, but also cosmic-ray particles undergo a similar process. When high-energy protons and nuclei (the primary components of cosmic rays) interact with atmospheric molecules, they initiate hadronic processes that predominantly produce neutral and charged pions. Neutral pions decay almost immediately into pairs of gamma rays, while charged pions undergo a sequential decay process, ultimately yielding electrons, positrons, and neutrinos. These interactions also generate extensive air showers that exhibit a complex composition that combines both hadronic and electromagnetic components. A key distinction between these components lies in their spatial distribution and development(shown in Figure 4.4). Hadronic interactions are characterized by significant transverse momentum transfer, leading to broader and more irregular shower structures compared to the more compact and predictable electromagnetic cascades produced by gamma rays. This difference arises because electromagnetic showers result

primarily from pair production and bremsstrahlung, which follow a more symmetric and constrained propagation pattern. The presence of hadronic cosmic rays thus introduces a substantial background in astrophysical observations, complicating the detection and analysis of purely electromagnetic signals generated from high-energy gamma rays. Hence, identifying the differences between electromagnetic and hadronic cascades becomes one of the main targets of ground-based γ-ray astronomy since the ratio of γ-rays to cosmic rays is extremely small. The methods of background separation will be discussed later in this paper.

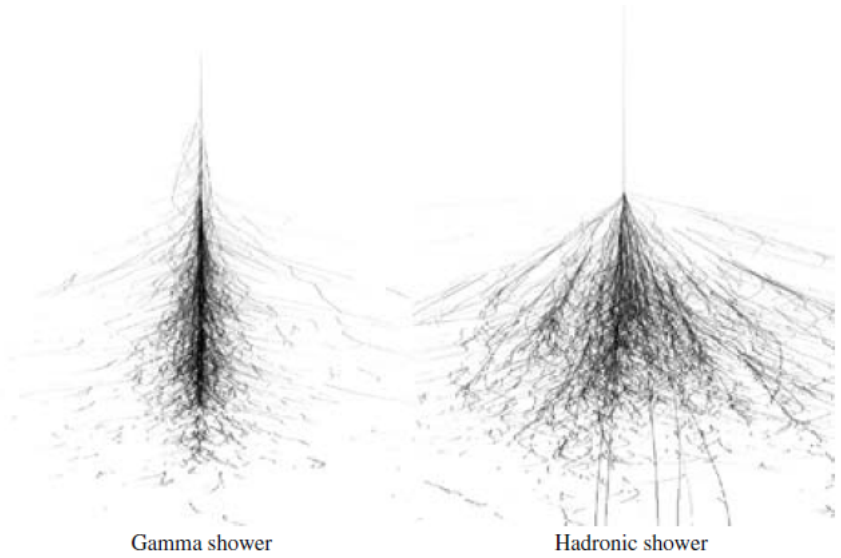

Figure 3.4: Schematic showing the difference in spatial distribution between a γ-ray induced shower and a hadron induced shower[*Völk and Bernlöhr, 2009*]

3.3.2 Air shower particle detectors and WCDs

To observe these extensive air showers, researchers employ ground-based arrays of particle detectors. Several key factors govern the overall sensitivity of such an array: its effective detection area across different energies, its capability to discriminate gamma-ray signals from the dominant cosmic-ray background, as well as its angular and energy resolution. The relative significance of each parameter varies depending on the nature of the gamma-ray source being investigated. The detector's energy response can be analyzed by applying a basic trigger condition and evaluating its efficiency as a function of both the primary gamma-ray energy and the detector's altitude. The spatial density of the sensitive detector elements plays a crucial role, as it determines the fraction of shower particles that are successfully recorded within the coverage area of the array. Consequently, a densely packed array typically achieves a lower energy threshold compared to a sparser configuration.

A common method for detecting air shower particles involves arrays of plastic

scintillators, typically covering $\sim$ 1m[*Errando and Saito, 2024*] surface areas with thicknesses of a few centimeters. These detectors are sparsely distributed over large areas to sample the extensive air showers. When electrons and positrons with energies as low as a few MeV pass through the scintillators, they produce measurable flashes of scintillation light, which are collected by photomultiplier tubes (PMTs). However, since scintillators only respond to charged particles, a significant fraction of the shower energy carried by photons remains undetected. To address this limitation, the scintillators are often covered with ~ 1[*Errando and Saito, 2024*] radiation length of lead or another high-atomic-number metal. This layer converts photons into detectable electron-positron pairs via pair production while minimally attenuating the existing charged particle flux. Prominent observatories utilizing scintillator arrays include the Chicago Air Shower Array (CASA), the Tibet Air Shower gamma experiment (Tibet-ASγ), and the Large High Altitude Air Shower Observatory (LHAASO), which leverage these detectors to study cosmic rays and gamma rays over vast detection areas.

Another approach for detecting air shower particles utilizes Cherenkov light emission in water, which can be collected by photomultiplier tubes (PMTs) submerged in large water volumes. The Milagro Gamma-Ray Observatory, operating at $2,630$m elevation in New Mexico, pioneered this technique by achieving an unprecedented 100GeV energy threshold[*Collaboration, 2004*]. It made landmark detections including the Crab Nebula, blazar Markarian 421[*Vernetto, 2012*], and Galactic diffuse emission before its 2008 decommissioning. One of the most pioneering WCDs is the High-Altitude Water Cherenkov (HAWC) Observatory located in Mexico. The HAWC Observatory has revolutionized our understanding of the VHE universe through its detection of over 100 gamma-ray sources across both galactic and extragalactic environments[*Collaboration, Albert, et al., 2020a*]. Its wide field-of-view and continuous monitoring capability have enabled groundbreaking studies of diverse astrophysical phenomena, including AGNs [*Collaboration, Albert, et al., 2021*], gamma-ray bursts [*Collaboration, Albert, et al., 2022*], and Galactic particle accelerators like PeVatrons [*Collaboration, Albert, et al., 2020b*] – potential sources of cosmic rays up to petaelectronvolt energies. The observatory has also made significant contributions to cosmic-ray physics through measurements of arrival direction anisotropies [*Abeysekara et al., 2019*], energy spectrum characterization, and composition studies.

3.3.3 Imaging Atmospheric Cherenkov Telescopes

The Imaging Atmospheric Cherenkov Technique takes advantage of the Cherenkov light(discussed in Section 3.3) emitted by the secondary atmospheric charged particles induced by photons or cosmic rays. Figure 3.5a shows how Cherenkov light is emitted at different heights in an air shower. The light is brightest from showers that develop between $10 - 20$km altitude. Although light from lower altitudes (the shower tail) has a wider emission angle, it travels a shorter distance

to reach the ground. Typically, this light spreads over a large area, about 300 meters across at 2200m altitude. This substantial spread enables detection of showers with large Impact Parameters(the perpendicular distance between the shower axis and detection point).

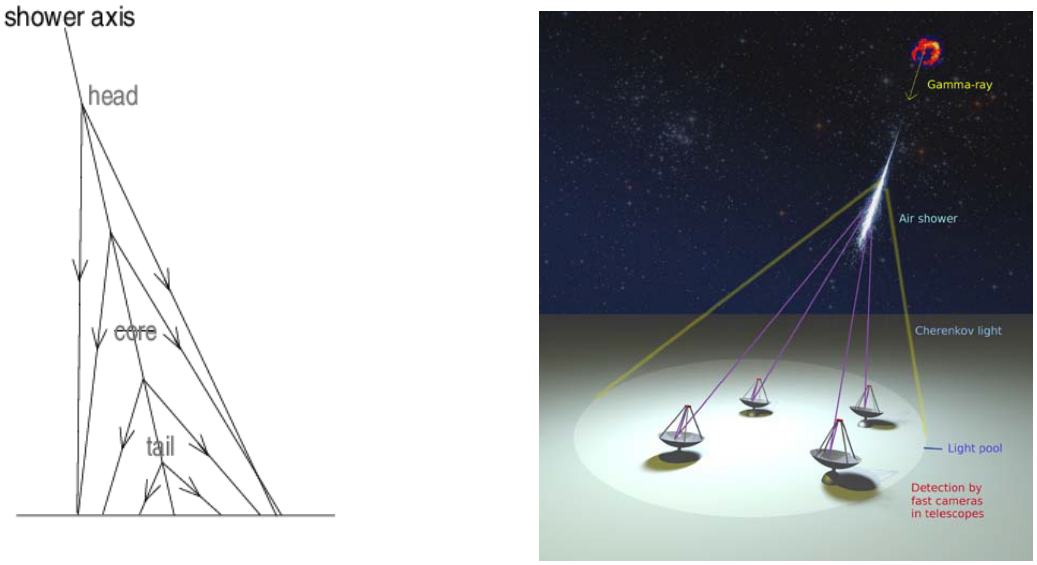

(a) (b)

Figure 3.5: Schematic of (a)Cherenkov light emission at different altitudes[*Prandini et al., 2023*], (b) a high-energy gamma ray from a cosmic source entering Earth's atmosphere, triggering an extensive air shower and illuminating an array of telescopes[*Völk and Bernlöhr, 2009*]

The IACTs detect the spatial distribution of Cherenkov light emitted by electromagnetic cascades in the atmosphere, allowing for the reconstruction of both the longitudinal and lateral development of air showers as well as the energy and arrival direction of the primary gamma rays. This method employs large optical reflectors (typically parabolic or spherical mirrors) that focus the faint Cherenkov photons onto high-sensitivity photomultiplier tube (PMT) arrays in the focal plane. This requires operation under dark, moonless conditions to maximize sensitivity to the nanosecond-scale light flashes. The principal advantage of the atmospheric Cherenkov technique lies in its capacity to achieve an exceptionally large effective collection area while simultaneously maintaining high angular and energy resolution.

Currently, there are three major IACTs in operation: The High Energy Stereoscopic System(H.E.S.S.) observatory located in the southern hemisphere, The Very Energetic Radiation Imaging Telescope Array System(VERITAS) and The Major Atmospheric Gamma-ray Imaging Cherenkov(MAGIC) located in the northern hemisphere.

3.4 The H.E.S.S. Telescopes

The H.E.S.S. is an array of five IACTs located in the Khomas Highlands of Namibia (23°16′18"S, 16°30′00"E) at an elevation of 1,835 meters. Designed to detect very high-energy gamma rays within an energy range of approximately 30GeV to 100TeV, H.E.S.S. began operations in 2003 with four telescopes (CT1–CT4) arranged in a square configuration with 120-meter sides as shown in Figure 3.6. Each of these telescopes features a 107m reflector and a camera equipped with 960 photomultiplier tubes (PMTs), providing a 5° field of view for high-resolution imaging of cosmic-ray-induced air showers.

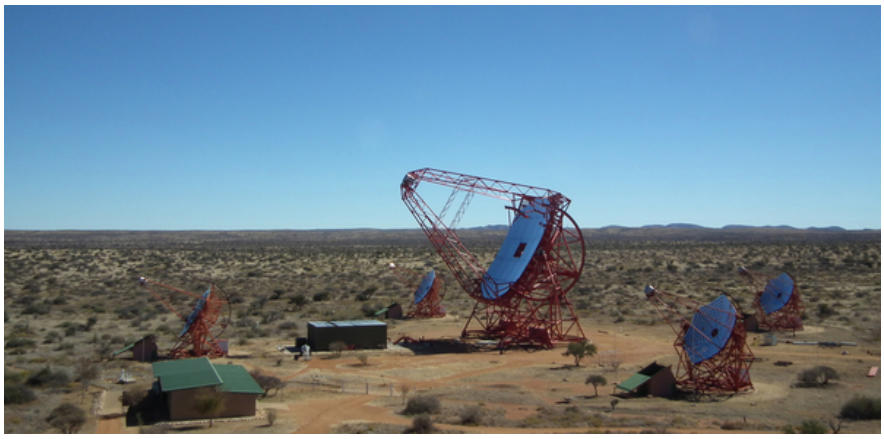

Figure 3.6: A layout of the 5 H.E.S.S. telescopes[*Hofman, 2012*]

In 2012, a fifth telescope (CT5) was installed in the center of the array to enhance the low-energy sensitivity of the system, reducing the threshold from 100 GeV to $\sim$ 30GeV. CT5 is equipped with a significantly larger 614m mirror, high-quantum-efficiency photosensors, and improved electronics to minimize dead time, enabling it to trigger on air showers at a rate of $\sim$ 3kHz, ten times higher than CT1–4. This upgrade allows H.E.S.S. to operate in two distinct modes: a stereoscopic mode, requiring coincident triggers from at least two telescopes for enhanced reconstruction accuracy, and a monoscopic mode, where CT5 operates independently to detect lower-energy events. As the world's first hybrid IACT array, H.E.S.S. combines the advantages of a large effective area, high event rate capability, and broad energy coverage, making it a cornerstone instrument in VHE gamma-ray astronomy.

3.4.1 Scientific achievements

Since its commissioning in 2003[*H.E.S.S. Collaboration, 2003*], the H.E.S.S. collaboration has made transformative contributions to very-high-energy (VHE) gamma-ray astronomy through groundbreaking discoveries across galactic and extragalactic sources. The experiment's 15-year survey of the Milky Way[*H.E.S.S.*

Collaboration, 2018a] revealed over 100 VHE emitters, including pulsar wind nebulae, supernova remnants, and previously unknown source classes like gamma-ray binaries and stellar bow shocks. Its Galactic Plane Survey[*Abdalla et al., 2018*], shown in Figure 3.7 provided the deepest view of the inner galaxy at teraelectronvolt energies, uncovering particle acceleration sites and mapping cosmic-ray interactions with interstellar matter. Notably, H.E.S.S. identified several "PeVatron" candidates through their hard spectra extending beyond 100TeV, offering crucial insights into the origins of Galactic cosmic rays up to the knee region ($\sim$ 1PeV)[*H.E.S.S. Collaboration, 2016*]

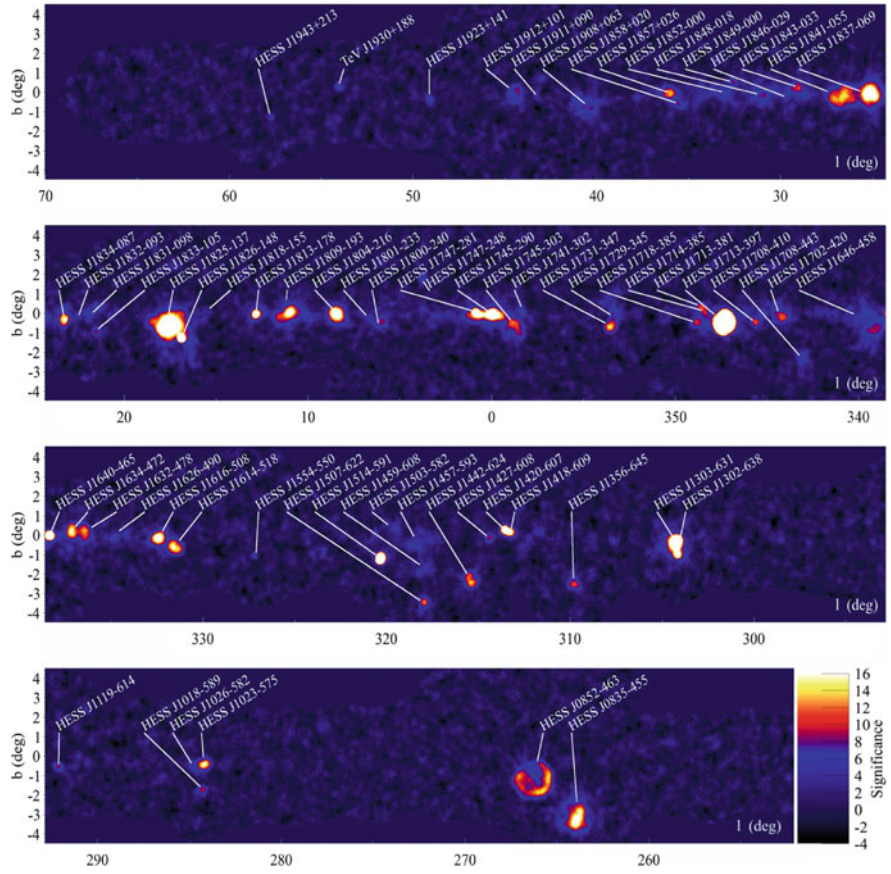

Figure 3.7: A significance map of the γ-ray sources in the galactic plane observed by H.E.S.S.[*Abdalla et al., 2018*]

H.E.S.S. has provided unparalleled insights into extragalactic particle acceleration through its studies of the radio galaxy Centaurus A. Combining Fermi-LAT (0.1–100GeV) and H.E.S.S. ($>$ 250GeV) data revealed a spectral hardening above $\sim$ 3GeV in the core emission, inconsistent with a simple power-law extrapolation[*H.E.S.S. Collaboration, 2018b*]. This deviation challenges single-zone synchrotron self-Compton models, suggesting either multiple emission zones or an additional accelerator.

Since initiating its Gamma-Ray Burst (GRB) observation program in 2008, the

H.E.S.S. collaboration has conducted follow-up observations for approximately 68 GRB alerts across diverse observational conditions. Significantly, 39 of these bursts were monitored using the large CT5 telescope, which provides the system's lowest energy threshold ($\sim$ 30 GeV) and highest sensitivity for detecting VHE emission. Despite this enhanced capability, no conclusive VHE gamma-ray signals were detected during either the prompt or afterglow phases of these events before August 2018[*Piel, 2019*]. Even though H.E.S.S. didn't detect any VHE gamma rays from these bursts at first, these "non-detections" were still extremely useful. They helped scientists fine-tune how H.E.S.S. responds to GRB alerts and analyze the data. These improvements paid off when H.E.S.S. made its first major discovery, catching high-energy gamma rays from GRB180720B. Together with MAGIC's detection of GRB 190114C[*Mirzoyan, 2019*], these findings have revolutionized our understanding of gamma-ray bursts. For the first time, scientists observed gamma rays with energies above 100GeV lingering long after the initial explosion, something earlier theories didn't expect. This forces us to rethink how particles accelerate in GRB jets and challenges long-standing models of how these cosmic explosions produce high-energy light.

4 Analysis of γ rays

The Cherenkov radiation observed by the H.E.S.S. telescopes must undergo a reconstruction process to extract information about the originating gamma-ray photon. This reconstruction involves analyzing the spatial and temporal properties of the detected Cherenkov light and employing these measurements to infer the energy and incoming direction of the primary gamma ray. The traditional technique for this purpose is the Hillas parameterization[*Hillas, 1985*], which characterizes air shower images using geometric and intensity-based parameters. This chapter provides a detailed examination of the Hillas analysis method, including the computation of its key parameters, the methodologies for energy and angular reconstruction, techniques for background rejection, and an assessment of the limitations in this approach.

4.1 The Hillas Method

As illustrated in Figure 4.1, a typical gamma-ray event captured by an IACT camera resembles an elliptical light distribution. The Hillas parameterization method involves computing the statistical moments of this elliptical image, which yield Hillas parameters, quantities that encode geometric, positional information, and orientation of the ellipse.

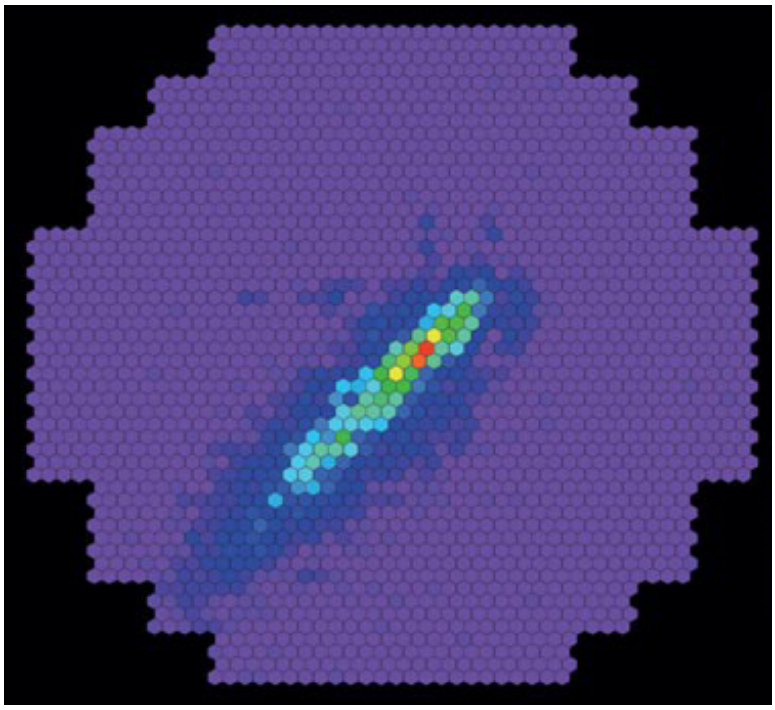

Figure 4.1: Gamma ray event recorded by one of the HESS telescopes

Measurable geometric properties characterize the elliptical shape of the Cherenkov

light image. The length and width of the ellipse correspond to its major and minor axes, which describe the longitudinal and lateral spread of the light distribution. The center of gravity (CoG) marks the intensity-weighted midpoint of the image, calculated from the brightness and positions of the camera pixels. The local distance measures how far this center is offset from the camera's central axis. The orientation of the ellipse is defined by two angles: α (alpha), the angle between the major axis and the line connecting the CoG to the camera center, and φ (phi), the direction of the major axis within the camera's coordinate system, which relates to the direction of arrival of the primary gamma ray. Figure 4.2 provides an illustration that identifies these parameters. The next section will go through the mathematical aspects of calculating the Hillas parameters.

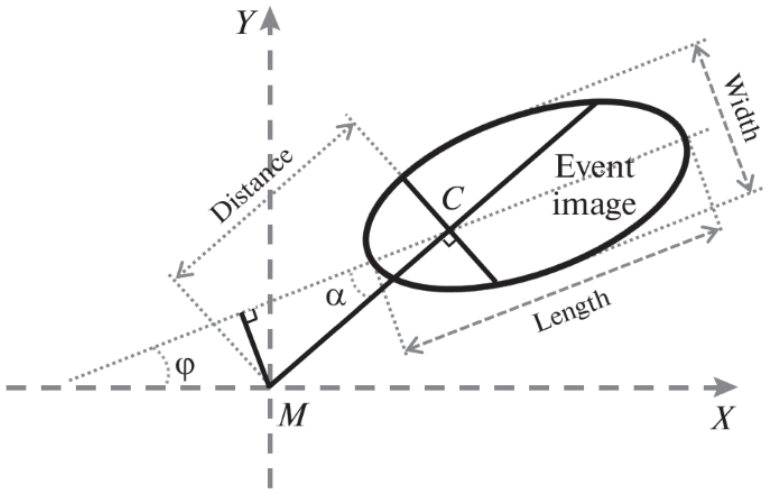

Figure 4.2: Schematic of an elliptical image visualizing the Hillas parameters[*Dubenskaya et al., 2023*]

4.2 The Hillas Parameters

When a gamma-ray shower is detected, each triggered pixel records three key pieces of information: its precise (x, y) coordinates within the camera plane and the intensity (or amplitude) a_i of each signal. The first step is to calculate the CoG coordinates of the image. This is computed separately for the dimensions x and y using intensity values as weights. Mathematically, this is expressed as:

$$\mathrm{CoG}_x = \frac{\sum x_i \cdot a_i}{\sum a_i} \tag{4.1}$$

$$\mathrm{CoG}_y = \frac{\sum y_i \cdot a_i}{\sum a_i} \tag{4.2}$$

where:

- x_i and y_i represent the coordinate positions of each triggered pixel
- a_i corresponds to the light intensity (typically measured in photoelectrons) recorded at that particular pixel
- The summation runs over all pixels that were activated by the event

Once the CoG coordinates are determined, the coordinate system is transformed to place the origin at this calculated center:

$$x_{\text{new}} = x_i - \text{CoG}_x \tag{4.3}$$

$$y_{\text{new}} = y_i - \text{CoG}_y \tag{4.4}$$

The arrival direction of the air shower is derived through analysis of the second-order spatial moments of the Cherenkov light distribution. The computation proceeds as follows: The second central moments of the intensity-weighted centroid are computed as:

$$S_{xx} = \frac{\sum_i a_i x_i^2}{\sum_i a_i} - \bar{x}^2 \tag{4.5}$$

$$S_{yy} = \frac{\sum_i a_i y_i^2}{\sum_i a_i} - \bar{y}^2 \tag{4.6}$$

$$S_{xy} = \frac{\sum_i a_i x_i y_i}{\sum_i a_i} - \bar{x}\bar{y} \tag{4.7}$$

These moments describe the spread and correlation of the intensity distribution in the x and y directions. The covariance matrix is given as:

$$\Sigma = \begin{bmatrix} S_{xx} & S_{xy} \\ S_{xy} & S_{yy} \end{bmatrix} \tag{4.8}$$

We define intermediate quantities:

$$r_k = S_{yy} - S_{xx} \tag{4.9}$$

$$r_l = \sqrt{r_k^2 + 4S_{xy}^2} \tag{4.10}$$

These are used to calculate the numerator and denominator for the angle expression:

$$\text{Numerator } (u) = (r_k + r_l) \sum_i a_i y_i + 2S_{xy} \sum_i a_i x_i \tag{4.11}$$

$$\text{Denominator } (d) = 2S_{xy} \sum_i a_i y_i - (r_k - r_l) \sum_i a_i x_i \tag{4.12}$$

The principal orientation angle φ is then given by:

$$\varphi = \tan^{-1} 2(u, d) \tag{4.13}$$

This angle enables the rotation of the coordinate system such that the x-axis aligns with the major axis (length) of the elliptical shower image and the y-axis aligns with the minor axis (width) as visualized in Figure 4.3. The coordinate transformation is given by:

$$x' = x_{\text{new}} \cos\varphi + y_{\text{new}} \sin\varphi \tag{4.14}$$

$$y' = -x_{\text{new}} \sin\varphi + y_{\text{new}} \cos\varphi \tag{4.15}$$

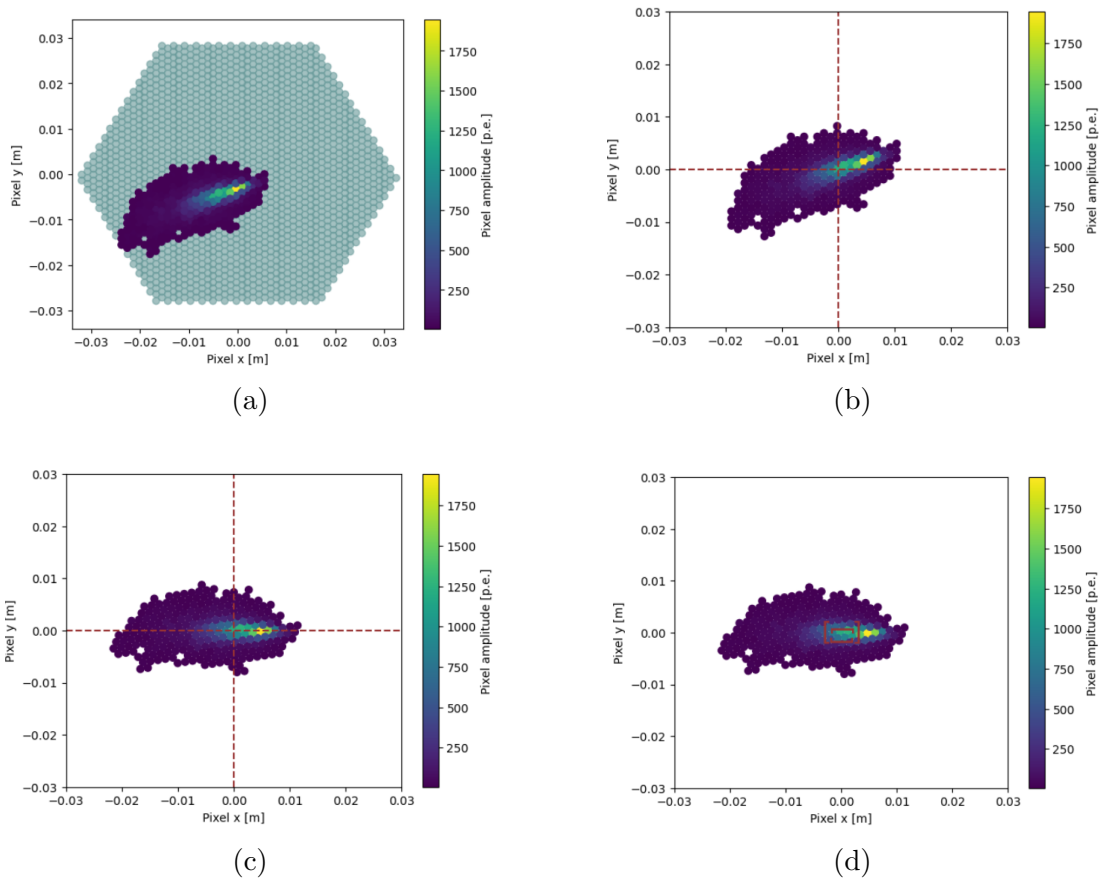

Figure 4.3: Step by step procedure of calculating the Hillas parameters visualized as (a) the original shower image, (b) the CoG coordinates calculated and the image transformed to the origin, (c) the direction calculated and the image rotated such that its major axis lies on the x-axis and (d) the final image with the shower length and width shown in red brackets

The n-th order moments of the distribution are defined in the rotated coordinate

system as:

$$\langle X'^n \rangle = \frac{\sum x_i'^n a_i}{\sum a_i} \tag{4.16}$$

The fundamental Hillas parameters - *length* and *width* - are derived from the second-order moments of the rotated distribution:

$$\text{Hillas length} = \sqrt{\langle X'^2 \rangle} \tag{4.17}$$

$$\text{Hillas width} = \sqrt{\langle Y'^2 \rangle} \tag{4.18}$$

Skewness: Skewness quantifies the asymmetry in the distribution, where a value of zero indicates perfect symmetry. The skewness of the rotated shower image is calculated as:

$$\text{Skewness} = \frac{\langle X'^3 \rangle}{\langle X'^2 \rangle^{3/2}} \tag{4.19}$$

Kurtosis: Kurtosis is defined as the measure of the sharpness of the curve, given by:

$$\text{Kurtosis} = \frac{\langle X'^4 \rangle}{\langle X'^2 \rangle^2} \tag{4.20}$$

These Hillas parameters serve as an important tool for energy and angular reconstruction. This will be discussed in detail in the following section.

4.3 Energy and Angular reconstruction

The camera image has been successfully characterized, yet essential information regarding the originating gamma ray remains undetermined. To recover this critical data, the shower must be reconstructed to infer the properties of the parent gamma ray. By determining the energy and arrival direction of the gamma ray, it becomes possible to trace its origin back to the astrophysical source. To achieve accurate reconstruction of the shower, including both energy and direction, a Neural Network is employed, which is trained on Monte Carlo simulations of gamma-ray events with predefined energies. The network utilizes the Hillas parameters derived from simulated shower images as input features, learning the underlying correlations between these parameters and the true gamma-ray energies through an iterative training process. The conventional H.E.S.S. analysis procedure employs a dual neural network system implemented using the `tensorflow.keras` deep learning framework.

For energy reconstruction, a Neural Network utilizes a set of Hillas variables: Hillas length, Hillas width, Hillas skewness, Hillas image amplitude, and Hillas logdensity as input to model the relationship between shower characteristics and gamma-ray energy. The network is trained for up to 2000 epochs on simulated gamma-ray events with known ("true") energies, allowing it to learn the underlying patterns and correlations. Once trained, the Neural Network predicts reconstructed energies,

which are then evaluated against the true energies to assess reconstruction accuracy. Key performance metrics, such as bias and energy resolution, are computed to quantify any systematic deviations or dispersion in the predictions. Crucially, an accurate reconstruction depends on the precise determination of the shower ellipse properties, as these parameters fundamentally influence the network's ability to infer the original gamma-ray energy.

Bias measures the systematic deviation from true energies, and Resolution measures the spread of the reconstructed energies. They are calculated as follows:

$$\text{Bias} = \left\langle \frac{E_{\text{Reco}} - E_{\text{True}}}{E_{\text{True}}} \right\rangle \tag{4.21}$$

$$\text{Resolution} = \sigma \left(\frac{E_{\text{Reco}} - E_{\text{True}}}{E_{\text{True}}} \right) \tag{4.22}$$

The Bias and Resolution plots for both the methods will be shown and discussed in the next chapter.

Similarly to energy reconstruction, a Neural Network is employed to estimate the disp parameter, the angular distance between the shower centroid and a known source position in the camera plane. The network is trained on simulated gamma-ray events where the true disp values are known, allowing it to learn the relationship between shower image features and the actual displacement. Once trained, the model predicts the reconstructed disp values, which, along with the measured shower centroids, are used to calculate the position of the source on the camera. The calculation depends on the skewness of the shower image, which determines the directionality of the gamma-ray arrival. The mathematical formulation is as follows:

If the corresponding Skewness value is < 0:

$$c_{\text{reco},x_i} = \text{CoG}_{x,i} + \text{disp}_{\text{reco},i} \cdot \cos(\varphi_i) \tag{4.23}$$

$$c_{\text{reco},y_i} = \text{CoG}_{y,i} + \text{disp}_{\text{reco},i} \cdot \sin(\varphi_i) \tag{4.24}$$

If the corresponding Skewness value is > 0:

$$c_{\text{reco},x_i} = \text{CoG}_{x,i} - \text{disp}_{\text{reco},i} \cdot \cos(\varphi_i) \tag{4.25}$$

$$c_{\text{reco},y_i} = \text{CoG}_{y,i} - \text{disp}_{\text{reco},i} \cdot \sin(\varphi_i) \tag{4.26}$$

where:

1. c_{reco,x_i}, c_{reco,x_i} are the reconstructed x, y coordinates of the source position
2. $\text{disp}_{\text{reco},i}$ is the reconstructed disp values
3. $\text{CoG}_{x,i}$, $\text{CoG}_{y,i}$ are the x, y Hillas centroid coordinates of the images

4. φ is the Hillas direction of the images

The reconstructed source positions are compared with the known true positions from Monte Carlo simulations to assess the performance of the reconstruction. This is done by calculating the angular distance between the known source position and the reconstructed source position and plotting the distance as a function of energy.

4.4 Background rejection

As discussed in section 3.2, one of the biggest challenges of ground-based detectors is background(in this case, hadronic showers) separation. As seen in Figure 4.4, gamma-ray showers produce cleaner, more compact elliptical patterns in the camera compared to the messier, more spread-out images from cosmic rays. The Hillas width and length parameters, exhibit statistically significant differences between the two shower types due to fundamental differences in their development processes.

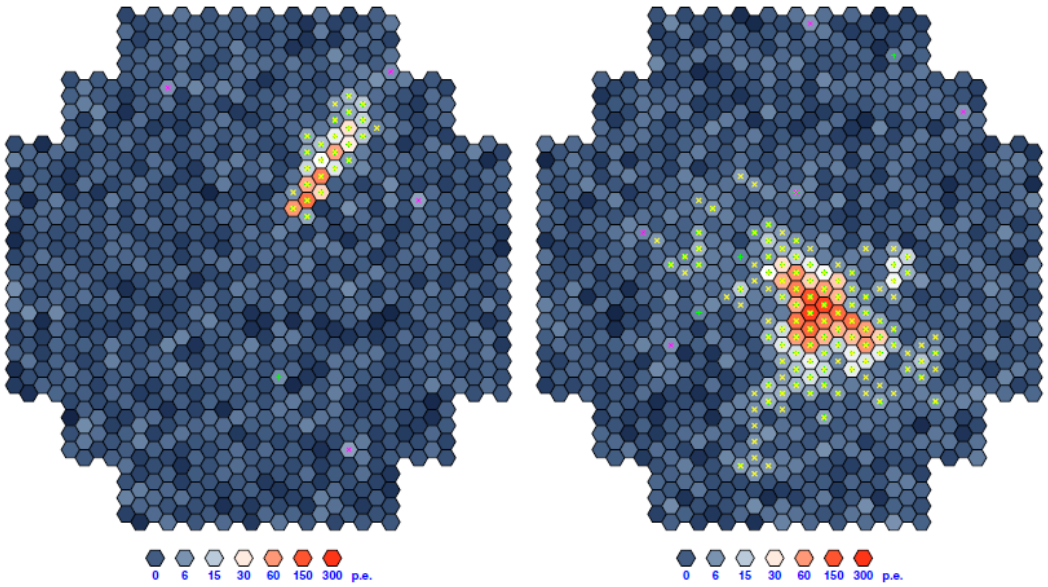

Figure 4.4: The difference between a gamma ray induced shower(left) and a hadronic shower(right)[*Völk and Bernlöhr, 2009*]

The analysis process involves a two-step background rejection process[*Berge et al., 2007*] to isolate the gamma-ray events from the hadron showers. In the first stage, optimized selection criteria are applied to the Hillas parameters, with different cut configurations (loose, standard, and hard) tailored for specific scientific objectives. For enhanced discrimination, the analysis incorporates machine learning algorithms, particularly Boosted Decision Trees (BDTs), which utilize the full

correlation structure of the Hillas parameters along with additional image characteristics. These BDTs are trained on comprehensive sets of simulated gamma-ray events and actual background data, producing a continuous discriminant (the zeta parameter) that quantifies the gamma-ray likeness of each event. The threshold for this parameter (typically zeta > 0.8)[*H.E.S.S. Collaboration, 2012*] is carefully optimized through studies of the quality factor, which evaluates the trade-off between signal efficiency and background rejection. Finally, any remaining background is subtracted using specialized methods that compare the source region to carefully chosen background regions.

4.5 Limitations

The Hillas parameterization, while a powerful tool for analyzing air-shower images in gamma-ray astronomy, has a fundamental limitation: it relies on the assumption that the Cherenkov light distribution is perfectly elliptical. This makes it unsuitable for truncated shower images, where part of the shower falls outside the camera's field of view as shown in Figure 4.5. When the light pool extends beyond the camera's edge, the resulting image is artificially clipped, distorting key parameters such as the shower's width, length, and centroid position. Since Hillas moments assume full light containment, this truncation introduces biases in reconstructing both the shower's arrival direction and energy. These biases become particularly problematic for high-energy showers or telescopes with narrow fields of view, where truncation effects are more pronounced.

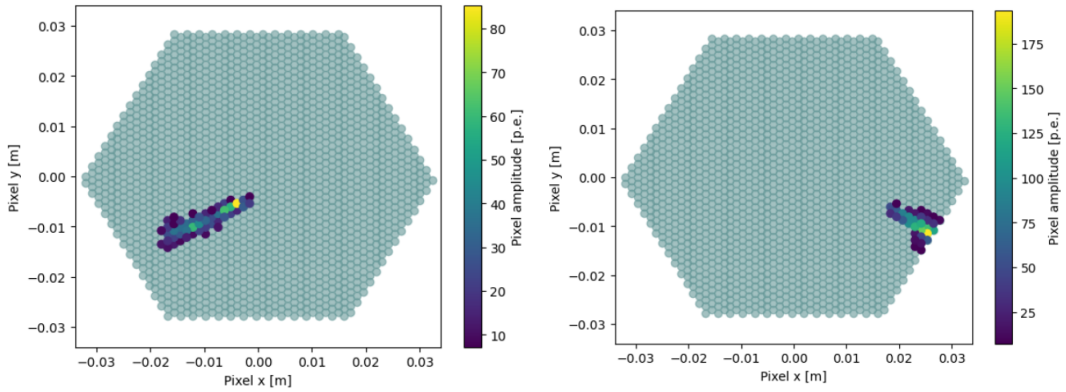

Figure 4.5: Two shower images showing the difference between a fully detected event(left) and a truncated event(right)

The degree of truncation depends on several factors. First, the impact distance, which is the perpendicular distance between the shower's core and the telescope, plays a crucial role. Showers with larger impact distances are more likely to be truncated, as their light pools spread over a wider area. Figure 4.6 displays the relationship of Hillas length and local distance with impact distance across three

distinct energy bins. The plots reveal two key trends: first, the local distance systematically increases with larger impact distances, reflecting the expected geometric expansion of the air shower footprint on the ground. More notably, the Hillas length exhibits a non-monotonic behavior, initially following the expected correlation with impact distance before decreasing beyond a certain threshold. This reversal occurs because showers with large impact parameters are more likely to be truncated at the edges of the camera's field of view, reducing the Hillas calculated length despite the shower's physical extent. Secondly, the energy of the primary gamma particle influences truncation: higher-energy showers produce broader Cherenkov light distributions, increasing the chance that part of the shower spills beyond the camera's edge. Finally, the telescope's field of view is a determining factor, cameras with smaller fields of view (such as the smaller HESS I telescopes) are more prone to truncation than those with wider fields (like the larger HESS II telescope).

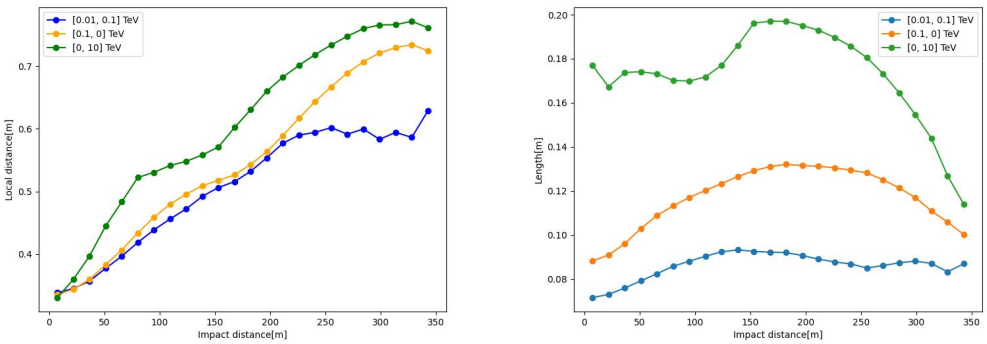

Figure 4.6: (a) Linear correlation between local distance and impact parameter across three energy ranges (colored bands), demonstrating the expected geometric expansion of air showers. (b) Non-monotonic relationship between Hillas length and impact parameter, where initial linear growth transitions to decreasing length measurements beyond $\sim$ 150m due to increasing image truncation at large impact distances. The energy-binned presentation demonstrates how this effect varies across different shower sizes.

To quantify the severity of truncation, two edge parameters (EP1 and EP2) are introduced as shown in Figure 4.7. EP1 measures the fraction of the total shower light detected in the outermost pixel ring of the camera, while EP2 extends this measurement to include both the outermost and the penultimate pixel rings. These parameters help assess how much of the shower's light is concentrated near the camera's edge. If EP1 or EP2 is close to zero, the image is fully contained, whereas values approaching one indicate severe truncation. The calculation of these parameters relies on summing the light amplitudes in the respective pixel rings and normalizing them by the total image amplitude.

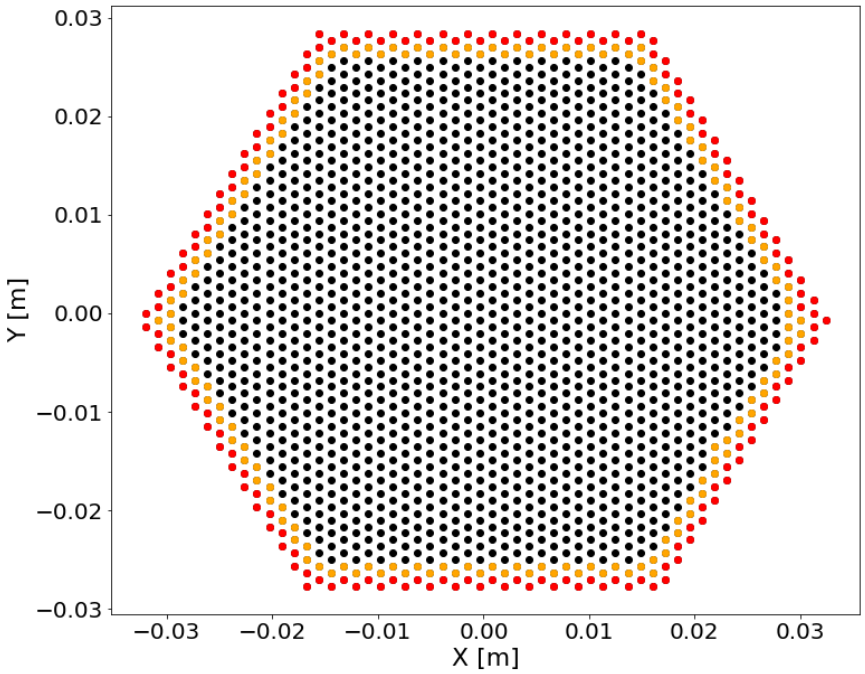

Figure 4.7: Schematic of a detectors camera showing its pixels. The outermost pixels are highlited in red while the penultimate pixels are in yellow.

When truncated images are analyzed using Hillas moments, systematic biases arise due to the missing light distribution. The most significant effect is the shift in the centroid position, since light is cut off at the edges, the reconstructed center of gravity moves inward toward the camera's center. This distortion affects the estimated major axis orientation, which is crucial for determining the arrival direction of the shower. Additionally, the total image amplitude is underestimated, leading to an incorrect energy reconstruction. Because of these biases, truncated events are often discarded in conventional analyses, reducing the effective detection efficiency, particularly for high-energy showers or telescopes with limited fields of view. However, the Hillas method remains widely used due to its computational efficiency, making it essential to understand its limitations when analyzing gamma-ray data.

This work focuses on developing an improved method for reconstructing air-shower images, particularly those that are truncated. Unlike conventional methods such as the Hillas parameterization, which rely on complete light containment, our approach aims to mitigate biases introduced by truncated events, thereby improving the reconstruction of shower direction and energy. By optimizing this method, we seek to enhance the sensitivity of HESS telescopes(or IACTs in general) to gamma-ray showers that would otherwise be discarded due to partial detection.

5 Asymmetrical Gaussian Fit

To address the limitations of the Hillas parameterization in handling truncated shower images, we introduce an advanced reconstruction technique based on an asymmetric 2D Gaussian model. The Hillas method characterizes showers using discrete moments (width, length, orientation, etc) calculated from pixel amplitudes, while the Gaussian approach fits a continuous asymmetrical 2D function with seven free parameters (centroid x/y, σ_x, σ_y, rotation φ, amplitude A, skewness α).

The asymmetric Gaussian function is defined as:

$$G(x,y) = A \cdot \underbrace{\exp\left(-\frac{x''^2}{2\sigma_x^2} - \frac{y''^2}{2\sigma_y^2}\right)}_{\text{Symmetric Gaussian}} \cdot \underbrace{\left[1 + \operatorname{erf}\left(\frac{\alpha x''}{\sigma_x\sqrt{2}}\right)\right]}_{\text{Asymmetry correction}} \tag{5.1}$$

Here, the first term represents a **standard 2D Gaussian**, which describes the symmetric spread of light, while the second term introduces a **skewness correction** via the error function (erf). The rotated coordinate frame (x'', y'') ensures that the Gaussian aligns with the shower's principal axis:

$$x'' = (x - m_x)\cos\theta + (y - m_y)\sin\theta \tag{5.2}$$
$$y'' = -(x - m_x)\sin\theta + (y - m_y)\cos\theta \tag{5.3}$$

with parameters:

- (x, y): Pixel coordinates of the shower image in the camera plane.
- (m_x, m_y): Centroid position of the shower image.
- (σ_x, σ_y): Standard deviations along the major and minor axes, corresponding to the length and width of the shower.
- A: Amplitude, representing the peak brightness of the shower.
- θ: Rotation angle that aligns the Gaussian with the shower axis.
- α: Skewness coefficient, controlling the direction and strength of asymmetry.

The error function term modifies the Gaussian shape along the major axis, allowing the model to adapt to asymmetric showers. The skewness parameter α plays a crucial role in determining the asymmetric properties of the Gaussian fit. When $\alpha > 0$, the error function term introduces a right-skewed distortion to the light profile along the major axis (x''), and $\alpha < 0$ produces a left-skewed distribution. The magnitude of α controls the strength of this asymmetry, with larger absolute

values resulting in more pronounced skewness. Importantly, when $\alpha = 0$, the error function term reduces to unity, and the model reverts to a symmetric Gaussian distribution.

The Hillas parameterization characterizes air showers through geometric moments derived from pixel amplitudes, providing an efficient but constrained representation that can struggle with truncated events. In contrast, the asymmetrical Gaussian fit offers significantly greater flexibility by accommodating variations in the shower's lateral distribution, making it far more adept at characterizing incomplete or edge-truncated images. The asymmetric Gaussian model provides several key improvements compared to traditional symmetric fitting approaches. First, it offers better handling of truncated showers by accounting for and fitting the missing information, allowing the model to infer the probable light distribution in regions where the camera did not capture the full shower. Second, it reduces bias in centroid and orientation determination; unlike Hillas moments, which shift inward when truncation occurs, this method maintains more accurate estimates of the shower's true centroid and major axis. Third, the model improves the energy reconstruction since the fit accounts for missing light.

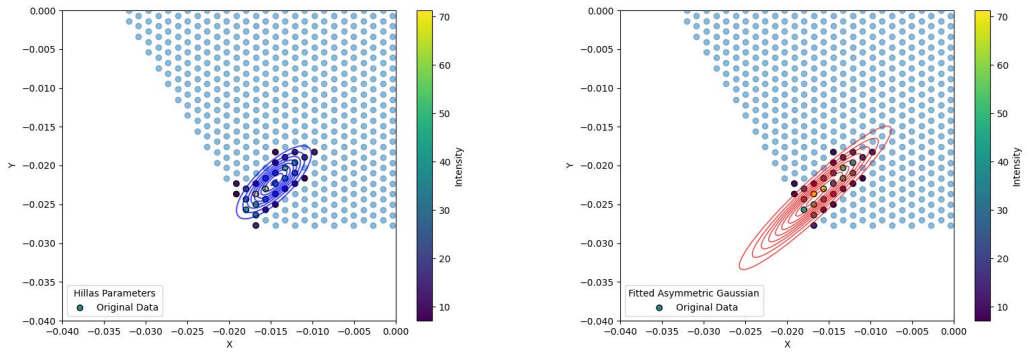

(a) (b)

Figure 5.1: (a) A truncated image fitted using Hillas parameters vs (b) fitted using asymmetric gaussian fit.

An example of this fitting process is illustrated in Figure 5.1, where the asymmetric Gaussian successfully reconstructs the expected light distribution, even when part of the shower is missing, while the Hillas parameters only account for the existing shower information. The figure demonstrates how the asymmetrical Gaussian fit extends in the appropriate direction, effectively "recovering" the truncated portion of the shower while maintaining agreement with the observed light distribution. This visual confirmation supports the mathematical formulation and shows the practical utility of the method for real observational data.

While the asymmetric Gaussian model shows promise, a detailed performance comparison with the Hillas method is necessary to quantify its advantages. Our

analysis will examine several key aspects: reconstruction accuracy for direction, energy, and shape parameters across different truncation levels (edge parameter values). This systematic evaluation will demonstrate where and to what extent the asymmetric approach outperforms traditional methods, providing concrete evidence for its adoption in gamma-ray astronomy analyses. The comparison will use simulated shower data with known gamma-ray energy values.

6 Hillas vs Asymmetrical Gaussian comparisions

This chapter presents a systematic comparison between the traditional Hillas parameterization(discussed in 4.2) and the proposed asymmetric Gaussian fitting method, using a dataset of simulated gamma-ray showers with precisely known energies. The simulations provide a controlled environment where the true shower properties are known, allowing for an objective evaluation of each method's reconstruction accuracy. For consistency, both techniques are applied to the same set of simulated events, ensuring a fair comparison. To focus on well-defined shower images, selection criteria are applied: only events with a total amplitude exceeding 300 photoelectrons ($\Sigma a_i > 300$) and at least 10 triggered pixels ($N_{a_i} > 10$) are included in the analysis. These cuts help eliminate faint or poorly sampled showers that could introduce unnecessary noise into the comparison.

The performance evaluation focuses on two critical aspects of shower reconstruction: energy estimation and angular resolution. Crucially, these comparisons are performed across different ranges of the edge parameter (EP), which quantifies the degree of image truncation. By binning events according to their EP values, we can isolate how each method performs for showers with varying levels of truncation—from fully contained images (EP ≈ 0) to severely truncated ones (EP $\rightarrow$ 1). This stratified analysis addresses the core objective of the thesis: to determine whether the asymmetric Gaussian method outperforms Hillas parameterization for truncated showers.

The datasets used consists of a combination of events with various truncation levels, making it essential to understand how truncation patterns vary across energy ranges for accurate methodological comparisons. Figure 6.1 presents the distribution of truncated versus non-truncated events across energy bins, revealing a clear and significant trend: non-truncated images overwhelmingly dominate at lower energies, while truncated events become progressively more prevalent as energy increases. In fact, at the highest energy levels, non-truncated images are virtually absent, with nearly all events exhibiting some degree of truncation.

Ultimately, this chapter validates the asymmetric Gaussian fitting method as a robust and reliable alternative for reconstructing truncated air showers. Through systematic comparisons with traditional approaches, the analysis not only confirms its superior performance in managing edge effects and incomplete images but also rigorously maps out its limitations. These findings provide essential guidance for its practical application, clearly delineating where the asymmetric Gaussian fit can be confidently applied and where alternative or complementary reconstruction techniques must be developed. By establishing both its strengths and boundaries, this work lays a foundation for future improvements in gamma-ray air shower analysis, ensuring more accurate and adaptable event reconstruction in next-generation experiments.

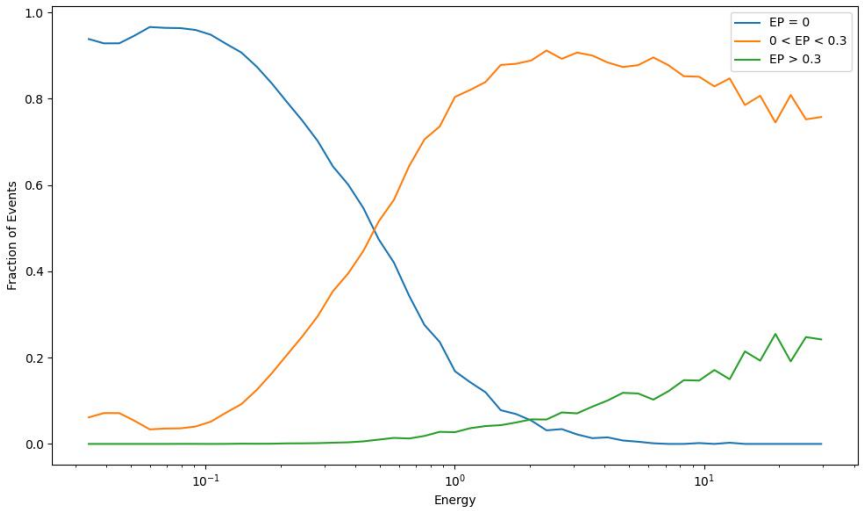

Figure 6.1: Plot showing the Fraction of events of various truncation levels vs the energy. This is explicitly for the dataset used in this work.

6.1 Hillas vs Asymmetrical Gaussian Parameters

This analysis begins by comparing three fundamental shower properties reconstructed by both methods: the position (Center of Gravity), size (length and width), and direction. The Center of Gravity (CoG) comparison, illustrated in Figure 6.2, demonstrates how the x and y coordinates differ between the asymmetric Gaussian fit and traditional Hillas parameterization, particularly highlighting their relative performance for truncated showers. The results are stratified by the severity of the truncation, $EP = 0$ (no edge effects), $0 < EP < 0.3$ (moderate truncation) and $EP > 0.3$ (strong truncation), to isolate how edge effects influence performance.

The results in Figure 6.2 demonstrate that the Hillas and Gaussian methods produce nearly identical CoG measurements for most events. However, significant differences emerge as the CoG positions move farther from zero. This systematic variation occurs because events near zero position represent central showers where the full light distribution is captured, allowing both methods to perform equally well. In contrast, events with larger offsets correspond to showers near the camera edges where truncation effects become prominent. The growing discrepancy at larger offsets suggests that the Gaussian method handles truncation more effectively by accounting for missing light, while the Hillas method becomes increasingly inaccurate for edge events due to incomplete images. Notably, these differences are minimal for events with zero edge parameter (non-truncated showers) and appear predominantly for events with positive EP values. This pattern confirms that the observed discrepancies are specifically caused by truncation effects rather than systematic biases between the two reconstruction methods.

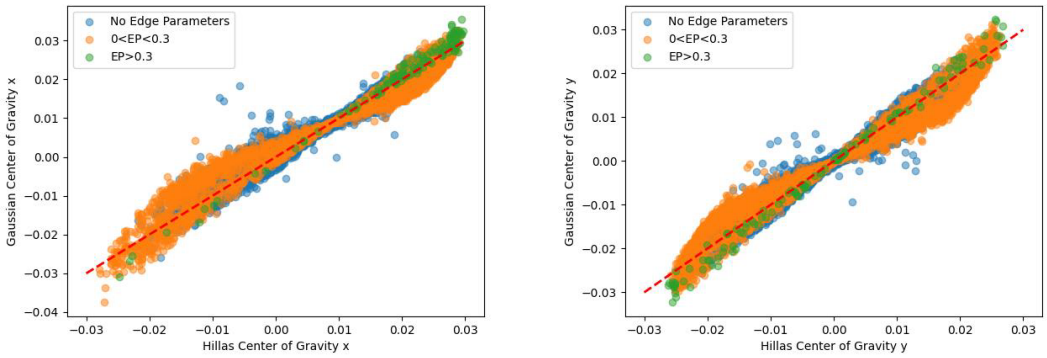

(a) (b)

Figure 6.2: Comparison plots between the Hillas calculated and asymmetrical Gaussian fitted (a) x-coordinate and (b) y-coordinate of the shower's centroid position

A similar comparison is done for the length and width measurements, presented on a logarithmic scale for clearer visualization.

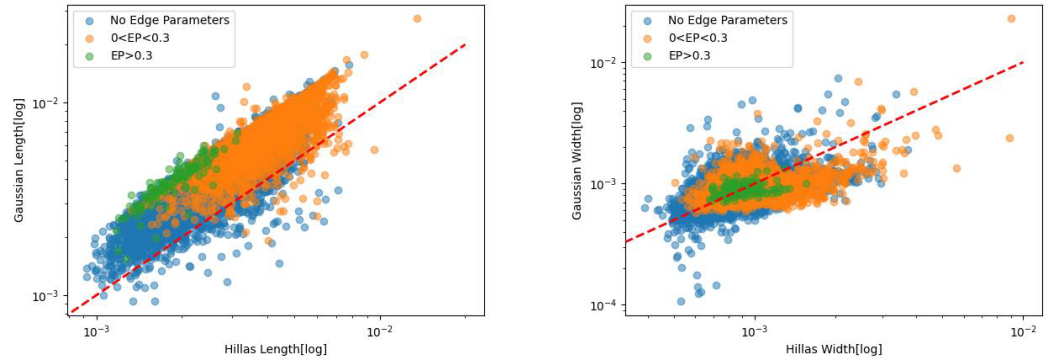

(a) (b)

Figure 6.3: Comparison plots between the Hillas calculated and asymmetrical Gaussian fitted (a) Length and (b) Width of the shower image

As shown in Figure 6.3, the asymmetric Gaussian method systematically produces longer length estimates than the Hillas approach, with the difference becoming particularly pronounced for events with positive edge parameter values. This consistent offset suggests the Gaussian method's skewness correction successfully accounts for truncated light distributions that would otherwise be missing from the analysis, while the Hillas method's symmetric fitting naturally underestimates lengths with positive EP values.

The width comparison plot reveals key differences between the Gaussian and Hillas methods when measuring shower dimensions. For non-truncated showers,

both methods show excellent agreement, with data points clustering tightly along the diagonal - this confirms the Gaussian method maintains consistency with traditional approaches for fully-contained events. However, as truncation increases, systematic differences emerge. In most cases, the Gaussian method estimates larger widths than Hillas, particularly for heavily truncated showers ($EP > 0.3$). However, systematic differences emerge as truncation increases. Moderately truncated showers (orange points, $0 < EP < 0.3$) show more scatter but generally follow the main trend, and heavily truncated events (green points, $EP > 0.3$) mostly lie above the diagonal.

The instances where the Gaussian fitting produces lower width estimates than the Hillas method can be attributed to its asymmetric correction along the shower's major axis. While the Gaussian model's skewness term (α, shown in (5.1)) primarily helps recover missing light for truncated images, this adjustment can sometimes lead to a tighter concentration of light along the minor axis (width direction). As the fit stretches the light distribution asymmetrically to compensate for truncation, resulting in longer reconstructed lengths, it may simultaneously produce a narrower profile perpendicular to this elongation. This occurs because the error-function-based correction redistributes light along the major axis, effectively "pinching" the lateral spread in some cases.

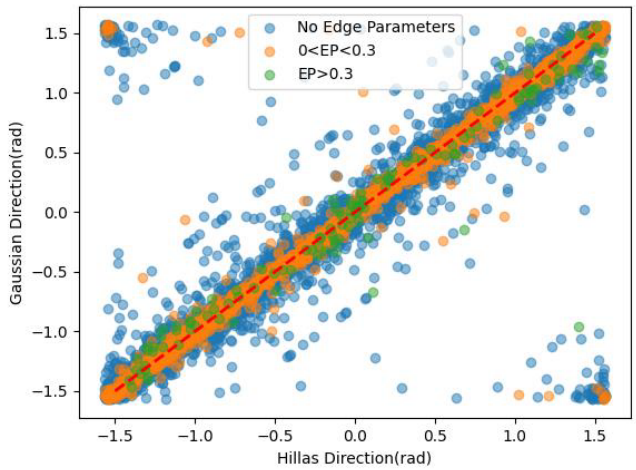

Figure 6.4: Comparison between the Hillas calculated and asymmetrical Gaussian fitted direction of the shower image

Figure 6.4 compares the shower direction estimates (in radians) reconstructed by the Hillas and Gaussian methods. For the majority of events, both methods produce consistent angular measurements, demonstrating reliable performance for well-contained showers where the light distribution is fully sampled. However, the plot reveals two notable types of discrepancies. First, a scattering of points shows minor deviations between the methods, likely caused by subtle differences

in how each technique handles edge effects or noise in partially truncated images. More strikingly, a distinct cluster of events appears where the two methods produce nearly opposite direction estimates (differing by $\sim \pi$ radians). These direction reversals are symmetrically distributed at both ends of the angular range, suggesting a systematic rather than random occurrence.

The π-radian discrepancies most frequently arise when analyzing highly symmetric shower images, where the elliptical light distribution lacks a clearly defined major axis orientation. In such cases, small asymmetries introduced by truncation or pixel noise can cause the fitting algorithms to arbitrarily select either of two possible, equally valid axis orientations 180 degrees apart. While both solutions are mathematically plausible for perfectly symmetric cases, only one corresponds to the true shower direction. This ambiguity affects both methods but may manifest differently depending on how each approach weights edge pixels or handles missing light. The presence of these flipped solutions highlights a fundamental challenge in reconstructing direction from elliptical shower images, particularly for events with near-perfect symmetry or significant truncation.

A comparison between Hillas and Gaussian parameters by dividing each Hillas parameter into equal intervals and calculating the mean value of the corresponding Gaussian parameter for events within each bin is demonstrated in Figure 6.5. This binned analysis visualizes the relationships discussed throughout the chapter, confirming that while both methods mostly agree for non-truncated showers, the Gaussian method produces larger length and width estimates for truncated events (particularly at higher edge parameter values). These binned comparisons quantitatively validate the key trends observed in the event-by-event analyses, demonstrating the Gaussian method's better handling of edge effects while maintaining consistency with Hillas for well-contained showers.

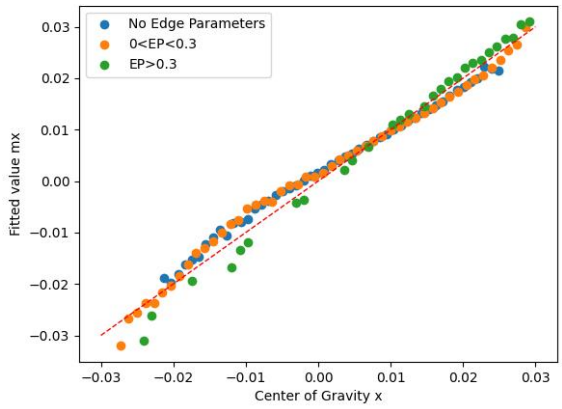

(a) Center of Gravity x coordinate

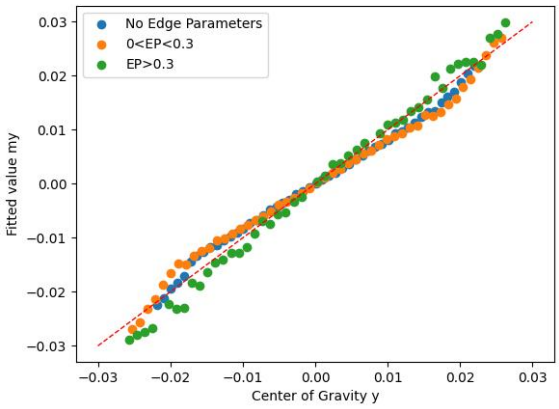

(b) Center of Gravity y coordinate

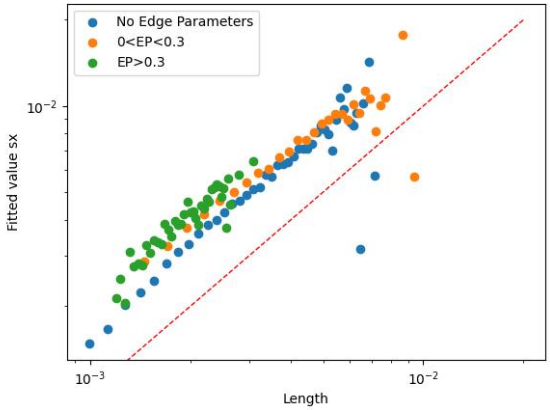

(c) Length

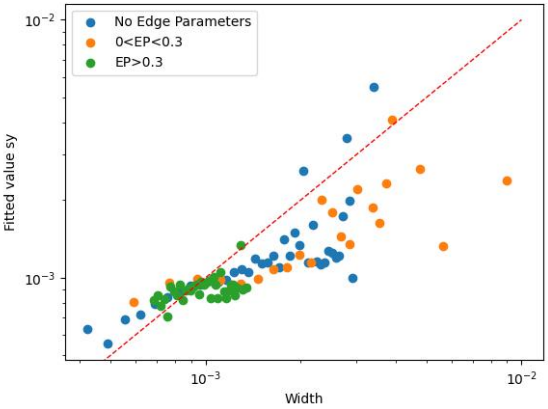

(d) Width

Figure 6.5: Comparison of shower reconstruction parameters between the Hillas and asymmetric Gaussian methods, showing the mean Gaussian parameter values (y-axis) calculated within equal-interval bins of Hillas parameters (x-axis)

6.2 Energy Reconstruction

To evaluate the performance of energy reconstruction, a neural network (as described in Section 4.3) was trained using Hillas and asymmetrical Gaussian parameters. Two-dimensional histograms were generated for each method comparing true versus reconstructed energies, with the results stratified by edge parameter (EP) values. Figure 6.6 reveals a clear systematic bias for truncated events, where both methods tend to underestimate the true energy.

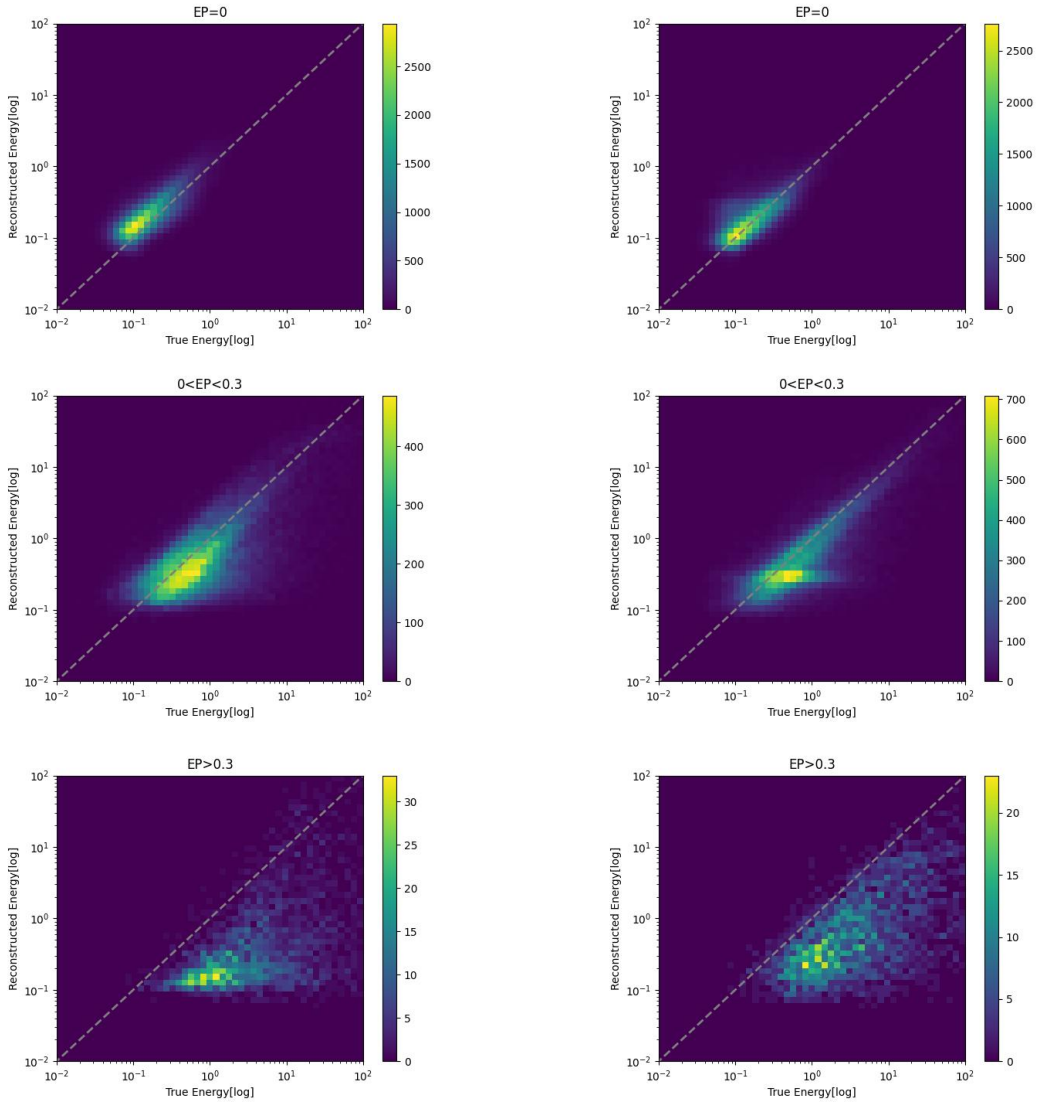

Figure 6.6: Two-dimensional histograms comparing true versus reconstructed gamma-ray energies in logarithmic scale for the Hillas (left) and asymmetrical Gaussian (right) reconstruction methods.

To address this issue, the neural network architecture was modified by incorporating the edge parameter (EP) as an additional input feature. This adjustment allows the network to explicitly account for truncation effects during the energy-reconstruction process. The 'edge parameter values' provide insights into the missing details in these truncated images, enabling the Neural Network to adjust and compensate for this loss of information. After retraining with this enhanced input set, the new reconstructed energies were compared to the true values for both methods. The improved results, as shown in Figure 6.7, show that including EP information helps mitigate bias, especially for moderately truncated showers ($0 < EP < 0.3$). However, some residual underestimation persists for severely

truncated events ($EP > 0.3$), suggesting that additional corrections or more sophisticated network architectures may be needed to fully compensate for extreme edge effects. These findings highlight both the potential and limitations of the Hillas parameterization and also the asymmetrical Gaussian fitting.

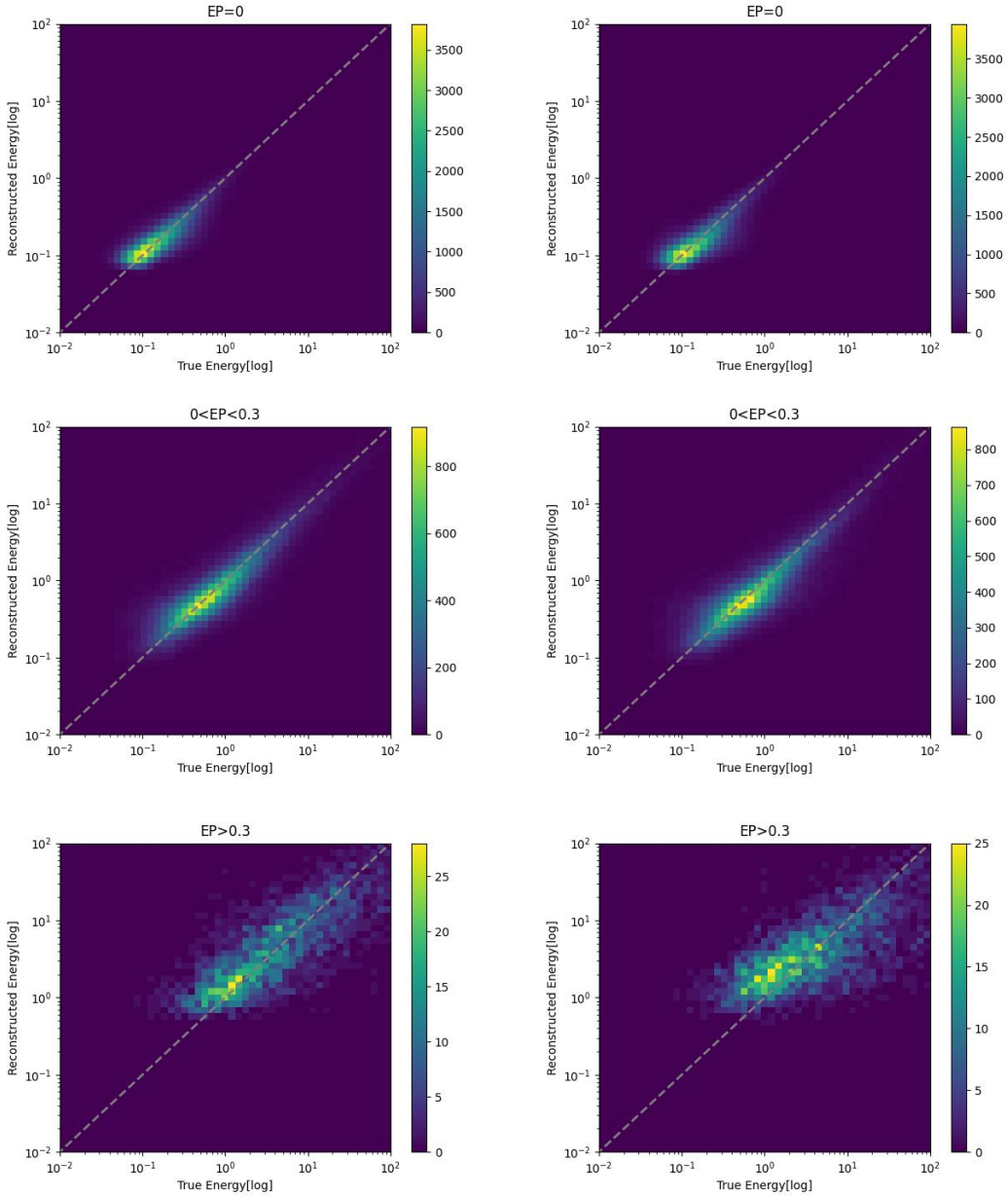

Figure 6.7: Two-dimensional histograms comparing true versus reconstructed gamma-ray energies for the Hillas (left) and asymmetrical Gaussian (right) methods, now incorporating the corresponding Edge Parameter values as input to the neural network.

To comprehensively evaluate the performance of both reconstruction methods, all

subsequent comparisons will analyze two distinct neural network configurations: one trained with traditional parameters alone, and another incorporating Edge Parameter (EP) values as additional input. This dual approach enables a direct assessment of how explicitly accounting for truncation effects improves the accuracy of energy reconstruction. By maintaining parallel analyses for both conditions, we can systematically identify which parameter set, Hillas or asymmetrical Gaussian, benefits most from EP inclusion, and determine the optimal combination for minimizing reconstruction errors. The accuracy of each method will be quantified through two key metrics: energy bias (the systematic deviation from true energies) and resolution (the statistical spread of reconstructed values). These metrics will be calculated across the full energy spectrum and stratified by EP ranges to isolate truncation-dependent effects.

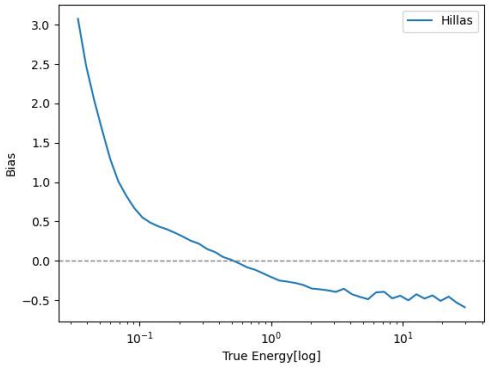

(a) Edge Parameters not included

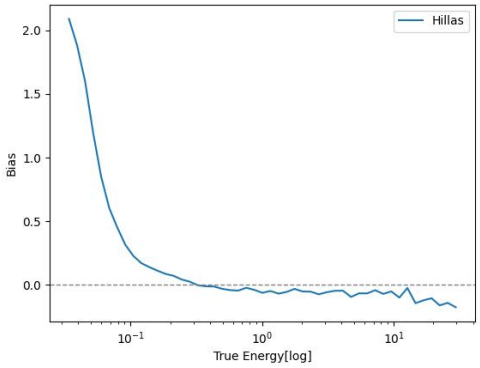

(b) Edge Parameters included

Hillas Method

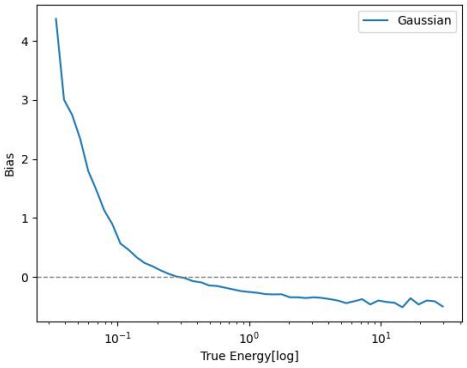

(c) Edge Parameters not included

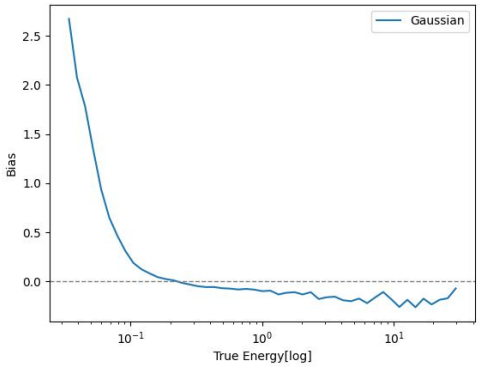

(d) Edge Parameters included

Asymmetrical Gaussian Method

Figure 6.8: Comparison of energy reconstruction bias versus true energy for the Hillas method(top) and the asymmetrical Gaussian fit(bottom), evaluated both with and without Edge Parameter inclusion in neural network training.

In an ideal scenario with perfect energy reconstruction, the bias plot would follow a horizontal line at zero across all energy values, indicating no systematic deviation from the true energies. However, reconstruction challenges—particularly at low energies—often distort this pattern. Low-energy events are more susceptible to truncation effects or may produce insufficient light for accurate analysis, typically resulting in larger biases. As shown in Figure 6.8, this manifests as a distinct trend: bias values are elevated at low energies but gradually converge toward zero as energy increases, reflecting improved reconstruction accuracy for brighter, well-contained showers. To further investigate truncation-dependent effects, Figure 6.9 stratifies the bias by different Edge Parameter (EP) levels, revealing how reconstruction errors scale with the severity of image truncation.

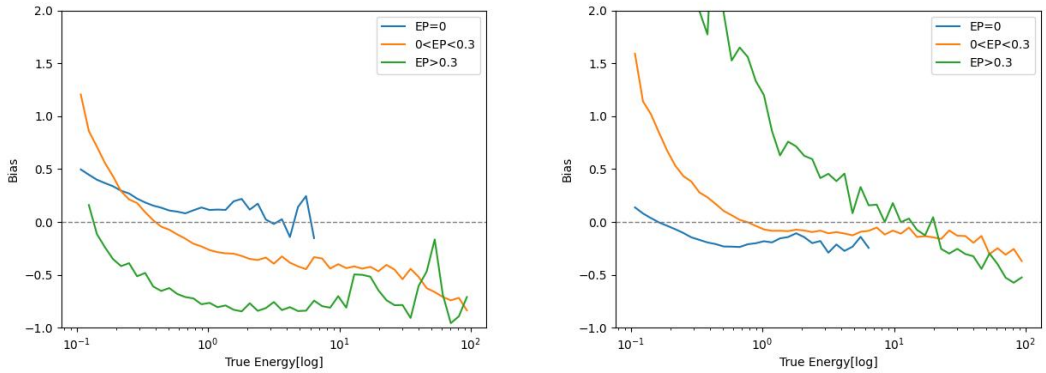

(a) Edge Parameters not included (b) Edge Parameters included

Hillas Method

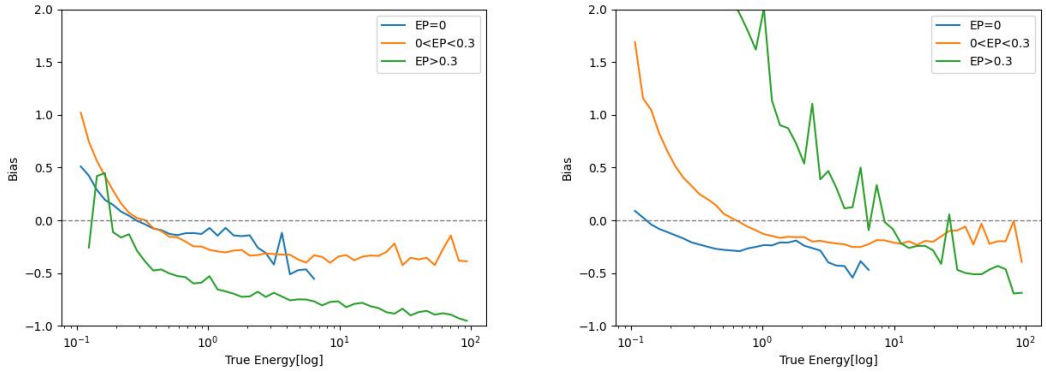

(c) Edge Parameters not included (d) Edge Parameters included

Asymmetrical Gaussian Method

Figure 6.9: Comparison of energy reconstruction bias versus true energy for the Hillas method(top) and the asymmetrical Gaussian fit(bottom), evaluated both with and without Edge Parameter inclusion in neural network training. The bias is calculated and plotted for different levels of truncation(EP values).

The plots in Figure 6.9 compare the energy reconstruction bias for the Hillas method and a neural network-based approach, evaluating two distinct training strategies: one that excludes edge parameters (EPs) and another that explicitly incorporates them in the training. Across all panels, the inclusion of EPs during training profoundly impacts the model's behavior, particularly for truncated events. This demonstrates that EP-aware training adapts the reconstruction to edge-induced distortions(this overall improvement can be seen in Figure 6.8), though the efficacy varies by energy range and truncation level.

When edge parameters are excluded (left panels a and c), a critical flaw emerges: events with strong truncation ($EP > 0.3$, green curves) exhibit a steepening negative bias as energy increases. This reveals that the NN underestimates energies for edge-affected showers, with growing severity at higher energies. The trend suggests the model, lacking truncation context, misinterprets missing edge light as lower total energy. In contrast, EP-inclusive training (right panels b and d) dramatically mitigates this issue. The green curve's negative bias at high energies flattens, showing the model now better accounts for lost light. However, this improvement introduces a compensatory effect: low-energy showers with $EP > 0.3$ now display a positive bias, indicating occasional overestimation.

A key observation is that the Asymmetrical Gaussian method consistently produces lower bias across most energy ranges and edge parameter conditions compared to the Hillas method. For example, when edge parameters are not included (plots a and c), the Asymmetrical Gaussian method (plot c) shows less pronounced bias, particularly for the $0 < EP < 0.3$ group (orange line), which remains more stable and less negatively biased than in the Hillas method (plot a). Similarly, when edge parameters are included (plots b and d), the Asymmetrical Gaussian method (plot d) again shows a more gradual and controlled bias trend, especially at higher energies, where the orange curve remains closer to zero than in the Hillas counterpart. This indicates that the Asymmetrical Gaussian method is inherently better at handling reconstruction near camera edges, even before considering edge parameters.

Notably, non-truncated events ($EP = 0$, blue curves) remain stable across both training schemes, confirming that EP inclusion specifically targets edge-related distortions without disrupting well-contained showers. Ultimately, these results advocate for EP-inclusive training as a better strategy. While imperfect, it yields a more balanced bias distribution overall, particularly for the most challenging truncated events.

The second key metric used for comparison is Resolution, which is illustrated in Figure 6.10 through plots of Resolution versus true energy for both reconstruction methods, with and without the inclusion of edge parameters in the neural network training. The behavior of Resolution closely mirrors that of Bias, exhibiting higher values at lower energies and progressively improving as energy increases. While all configurations show relatively poor resolution in the low-energy regime, the integration of edge parameters into the training process leads to a noticeable

enhancement in resolution at higher energies.

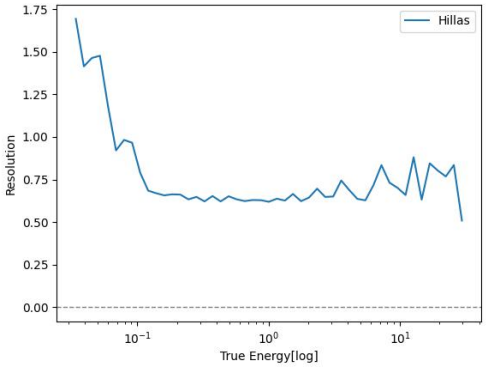

(a) Edge Parameters not included

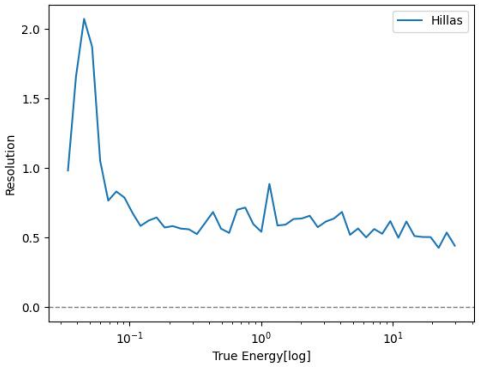

(b) Edge Parameters included

Hillas Method

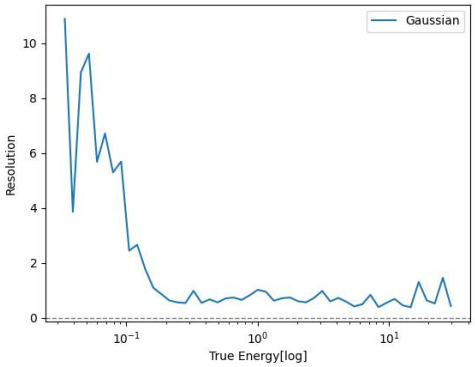

(c) Edge Parameters not included

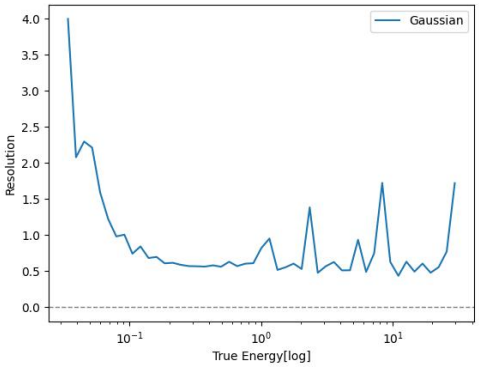

(d) Edge Parameters included

Asymmetrical Gaussian Method

Figure 6.10: Comparison of energy reconstruction resolution versus true energy for the Hillas method(top) and the asymmetrical Gaussian fit(bottom), evaluated both with and without Edge Parameter inclusion in neural network training.

The energy resolution of the reconstruction methods must be evaluated as a function of truncation severity, similar to the bias analysis. Figure 6.11 presents the resolution versus true energy for different EP ranges. The resolution improves at higher energies, particularly for moderately truncated showers ($0 < \text{EP} < 0.3$), where both methods perform similarly. For heavily truncated events ($\text{EP} > 0.3$), resolution degrades significantly, highlighting the need for improved reconstruction techniques to handle these images.

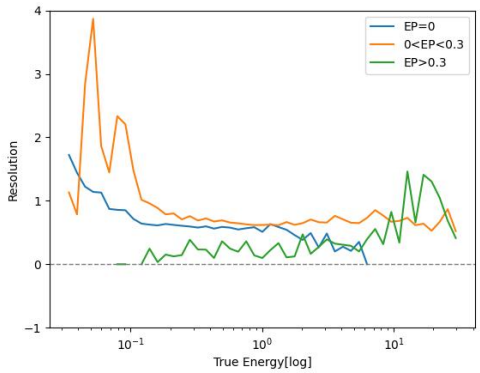

(a) Edge Parameters not included

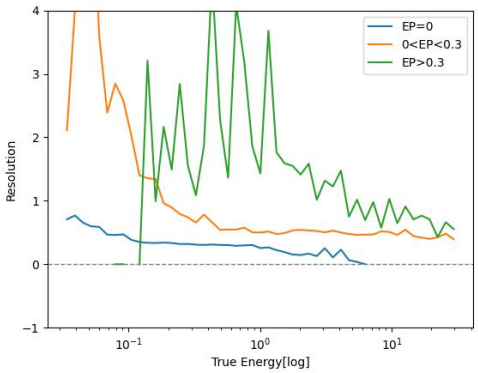

(b) Edge Parameters included

Hillas Method

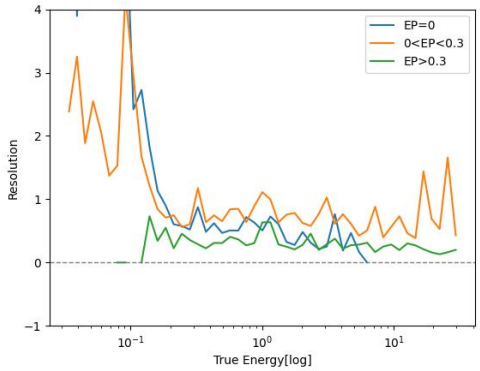

(c) Edge Parameters not included

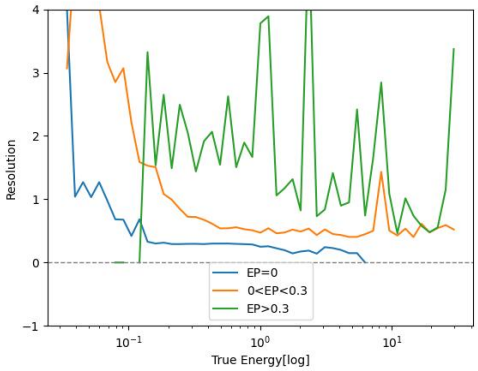

(d) Edge Parameters included

Asymmetrical Gaussian Method

Figure 6.11: Comparison of energy reconstruction resolution versus true energy for the Hillas method(top) and the asymmetrical Gaussian fit(bottom), evaluated both with and without Edge Parameter inclusion in neural network training. The resolution is calculated and plotted for different levels of truncation(EP values)

6.3 Angular Reconstruction

The evaluation of angular reconstruction accuracy focuses on how well the Hillas and asymmetrical Gaussian methods recover the true source position on the camera plane. This process depends mainly on three critical parameters: the calculated centroid and direction values, and the disp value, which is the angular distance between the centroid and the true source position. The disp values are reconstructed using a neural network trained similarly to Section 6.3. The neural network is trained under two distinct conditions: one excluding edge parameters (EPs) and another incorporating them, allowing us to isolate how truncation

awareness impacts positional accuracy. The final source coordinates are derived by combining the centroid, disp, and direction parameters, with adjustments based on the shower's skewness to account for asymmetrical light distributions(discussed in detail in section 4.3).

Using this method, the source position values are calculated for both the Hillas and asymmetrical Gaussian methods with their respective parameters. The reconstruction accuracy of both the Hillas and asymmetrical Gaussian methods is quantified by computing the angular distance between each reconstructed source position and its corresponding true position. To characterize the performance, the 68th percentile of these angular offset(a statistical measure that indicates the radius within which 68% of the reconstructed source positions fall relative to their true positions) is calculated and this metric is plotted as a function of energy, allowing an assessment of how reconstruction accuracy varies across different energy ranges. This energy-dependent analysis is particularly valuable, as lower-energy showers typically produce fainter and more diffuse images that are more challenging to reconstruct accurately, while higher-energy events generally yield more precise measurements.

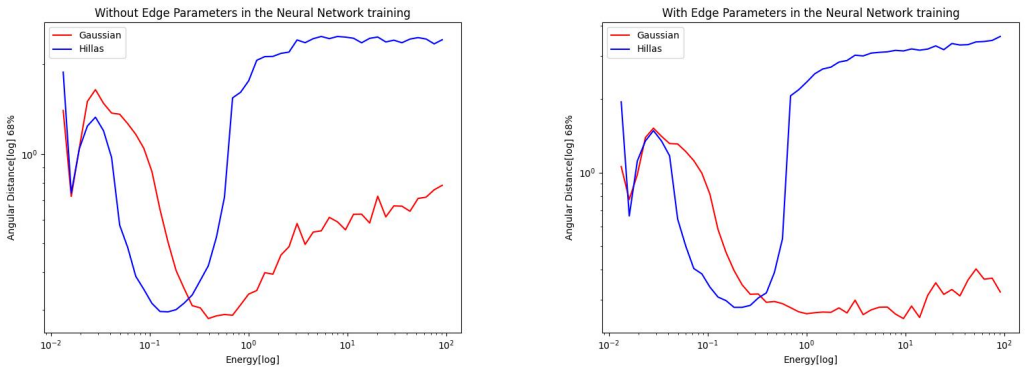

(a) (b)

Figure 6.12: (a) Comparison of source position reconstruction accuracy between the asymmetrical Gaussian and Hillas methods, without EP inputs in the neural network training. The 68th percentile angular resolution (y-axis) is plotted as a function of energy (x-axis). (b) Reconstruction performance with EP-aware neural network training.

In an ideal scenario with perfect reconstruction, the 68th percentile of angular distances between reconstructed and true source positions would approach zero, indicating flawless pointing accuracy. However, systematic biases emerge across the energy spectrum due to physical and geometrical constraints. At low energies, showers produce faint, compact images that challenge reconstruction algorithms, leading to significant angular offsets. The limited light pool and poor signal-to-noise ratio make precise centroid and direction determination difficult. As energy

increases, the bias typically diminishes due to brighter, more extended showers that yield better-sampled images, allowing both Hillas and asymmetrical Gaussian methods to converge toward the true position. At the highest energy ranges, the bias increases again, primarily because these energetic showers frequently produce large light pools that exceed the camera's field of view (high edge parameter values). This truncation effect distorts key parameters like the centroid and major axis orientation, particularly in symmetric Hillas reconstruction. Thus, the angular resolution follows a U-shaped trend versus energy: poorest at the low-energy regime (due to small shower size), optimal at intermediate energies (where showers are bright but not truncated), and degraded again at the highest energies (due to edge truncation). This trend is clearly visible for Hillas reconstruction in Figure 6.12.

The results demonstrate that the proposed asymmetrical Gaussian method consistently outperforms the traditional Hillas approach in angular reconstruction accuracy across both training configurations, with and without edge parameter inputs to the neural network. While both methods show expected degradation for truncated showers, the asymmetrical Gaussian maintains better resolution due to its inherent ability to model skewed light distributions through its shape parameters. The improvement becomes particularly dramatic when edge parameters are included in the training, compared to the EP-aware Hillas reconstruction. This enhanced performance stems from the method's dual advantages: (1) its physical skewness correction that better handles edge-clipped shower geometries, and (2) its synergy with EP-informed neural networks that learn truncation-specific corrections. The consistent superiority across all energy ranges and truncation levels confirms that the asymmetrical Gaussian parameterization more faithfully characterizes gamma-ray shower properties, especially in challenging cases where traditional Hillas analysis fails.

To better evaluate the performance gains, Figure 6.13 analyzes angular reconstruction across different edge parameter (EP) ranges. The results demonstrate that the asymmetrical Gaussian method achieves higher accuracy compared to Hillas parameterization across all truncation levels, with particularly striking improvements for moderately truncated showers ($0 < EP < 0.3$, green data points). At high energies (> 1TeV), where traditional Hillas analysis shows severe biases, the asymmetrical Gaussian maintains low resolution.

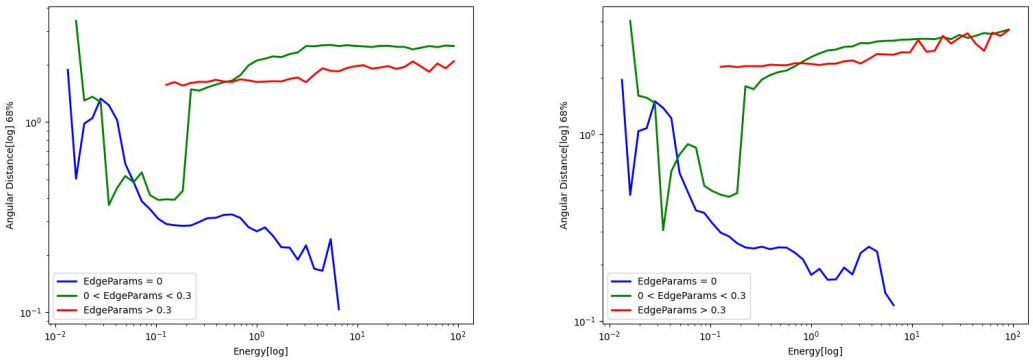

(a) Edge Parameters not included (b) Edge Parameters included

Hillas Method

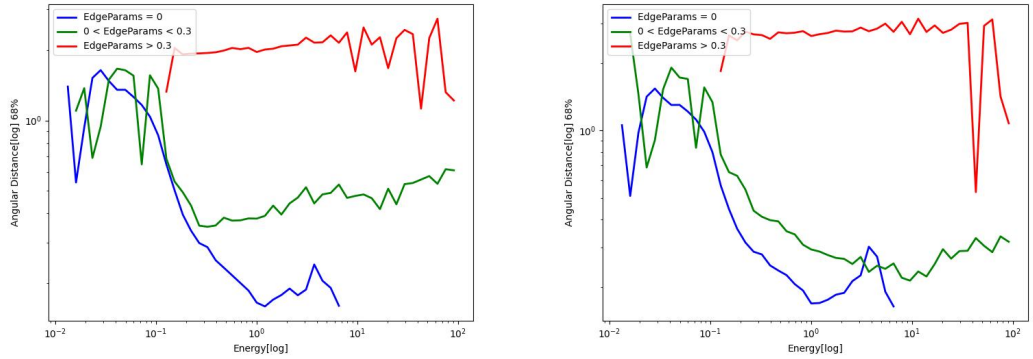

(c) Edge Parameters not included (d) Edge Parameters included

Asymmetrical Gaussian Method

Figure 6.13: Comparison of angular reconstruction bias versus true energy for the asymmetrical Gaussian and Hillas methods, evaluated both with and without Edge Parameter inclusion in neural network training. The bias is plotted for different levels of truncation(EP values)

However, both methods struggle with heavily truncated showers ($EP > 0.3$, red data points), where typically very few pixels record light at the extreme camera periphery. In these extreme cases, even the asymmetrical Gaussian's advanced parameterization cannot fully overcome the fundamental lack of topological information; the remaining light fragments often lack sufficient spatial or amplitude cues to reliably reconstruct the shower core or direction. While the asymmetrical Gaussian still shows better resolution than Hillas for these challenging events, their overall poor reconstruction quality suggests such showers should likely be excluded from scientific analysis when possible. This limitation highlights a physical boundary in IACT analysis where truncation becomes too severe for any current reconstruction method to overcome.

During shower reconstruction, a known challenge is the occasional production of *flipped* solutions, where the reconstructed source position appears on the opposite side of the centroid than physically expected. To quantify this phenomenon, the flip error rates across energy bins are calculated by analyzing events with positive skewness values (indicating a preferred directionality in the light distribution). A flip is identified when the reconstructed x-coordinate (x_{reco}) lies opposite to the predicted position relative to the centroid (x_{CoG}), specifically when:

$$x_{\text{reco}} > x_{\text{CoG}} \quad \text{for positively skewed showers} \tag{6.1}$$

This directional inversion typically occurs when the shower image exhibits near-perfect symmetry or when edge truncation removes critical directional cues. The flip error value represents the fraction of such misreconstructed events within each energy bin.

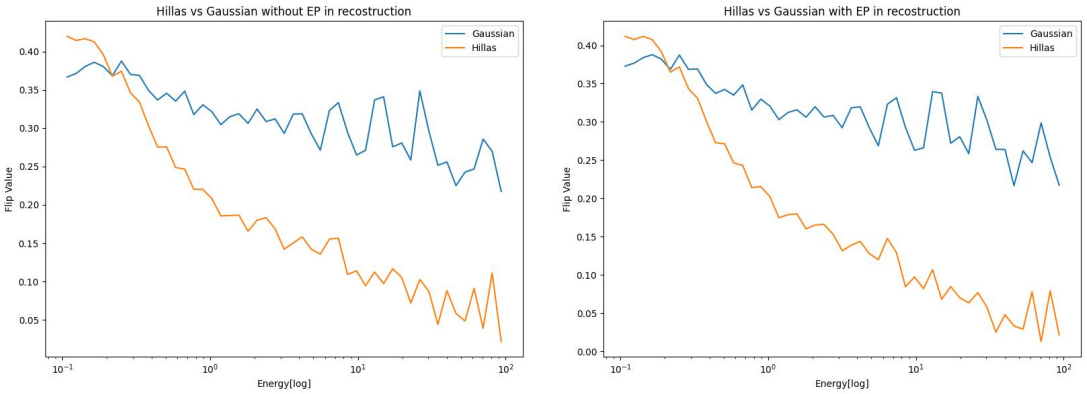

(a) (b)

Figure 6.14: Fraction of flip errors as a function of energy for both Hillas and asymmetrical Gaussian reconstruction methods. Results are shown for two neural network training conditions: without (a) and with (b) edge parameter (EP) inputs.

A comparison of the frequency of flip errors between the Hillas and asymmetrical Gaussian methods is shown in Figure 6.14. Contrary to typical performance trends in other reconstruction metrics, the asymmetrical Gaussian method exhibits a slightly higher flip error rate than Hillas parameterization across both neural network training conditions (with and without edge parameters). This counterintuitive result likely stems from the asymmetrical Gaussian's sensitivity to skewed light distributions: while its skewness correction improves energy and position reconstruction for truncated showers, it can overinterpret subtle asymmetries in near-symmetric images, occasionally forcing a preferred direction where the Hillas method remains ambiguous. The effect is most pronounced for high-energy showers. Despite this drawback, the asymmetrical Gaussian's overall improved accuracy in other reconstruction parameters (angular resolution, energy estimation) maintains its advantage for comprehensive shower analysis, though flip errors may require targeted mitigation for precise source localization.

7 Discussion and Conclusions

This study demonstrates that the asymmetrical Gaussian fit outperforms the conventional Hillas parametrization in reconstructing shower images, particularly in handling truncated data. When analyzing non-truncated images, both the Hillas and asymmetrical Gaussian methods yield comparable results, with their parameters aligning well. However, the key advantage of the asymmetrical Gaussian fit becomes evident in cases of image truncation, where it significantly improves parameter estimation by accounting for the missing data. Unlike the Hillas method, which does not adjust for truncation, the asymmetrical Gaussian approach effectively accounts for the lost information through its fitting, leading to more accurate determinations of the shower's size and centroid position. Additionally, while both techniques generally agree on the direction parameter for the majority of events, discrepancies arise in rare instances involving highly symmetric showers. In these cases, there is a possibility that either of the two methods may misidentify the major axis, leading to incorrect direction values.

While characterizing secondary shower images is not the primary focus of this study, the central objective is instead the accurate reconstruction of the parent gamma-ray's energy and angular properties. The second and most critical phase of this work involved utilizing the previously determined shower properties to estimate the parent gamma-ray's energy and source direction. Here, a new approach was introduced: incorporating edge parameters into the neural network training to enhance reconstruction accuracy. This new addition, combined with the already superior performance of the asymmetrical Gaussian method over Hillas parametrization, resulted in a significantly more effective tool for energy and angular reconstruction. The improvement is especially pronounced at higher energies, where image truncation becomes more frequent and problematic.

Despite its advancements, the improved asymmetrical Gaussian method still has notable limitations, particularly when dealing with extreme cases of image truncation (EP>0.3). In these severe truncation scenarios, the method's performance deteriorates for both energy and angular reconstruction, even with the enhanced neural network training that incorporates edge parameters. This suggests that while the technique is more resilient than the Hillas parametrization, it does not fully overcome the challenges posed by heavily truncated images. However, it is important to emphasize that such extreme truncation cases constitute only a small fraction ($\sim 1\%$) of the dataset used in this study, making it difficult to draw definitive conclusions about their impact. Consequently, future work will require a more sophisticated and refined analysis approach to address these high-truncation regimes, ensuring reliable reconstruction across all possible shower conditions. This highlights an important area for further development in gamma-ray shower reconstruction techniques.

Bibliography

Abdalla, H. et al. (2018). "The H.E.S.S. Galactic plane survey". In: *Astronomy & Astrophysics* 612, A1. DOI: 10.1051/0004-6361/201732098. arXiv: 1804.02432 [astro-ph.HE].

Abeysekara, A. U. et al. (2019). "All-Sky Measurement of the Anisotropy of Cosmic Rays at 10 TeV and Mapping of the Local Interstellar Magnetic Field". In: *The Astrophysical Journal* 871, pp. 96–116. DOI: 10.3847/1538-4357/aaf5cc.

Atwood, W. B., A. A. Abdo, M. Ackermann, W. Althouse, et al. (2009). "The Large Area Telescope on the Fermi Gamma-ray Space Telescope Mission". In: *The Astrophysical Journal* 697.2, pp. 1071–1102. DOI: 10.1088/0004-637X/697/2/1071.

Berge, D., S. Funk, and J. Hinton (2007). "Background modelling in very-high-energy γ-ray astronomy". In: *Astronomy & Astrophysics* 466, pp. 1219–1229. DOI: 10.1051/0004-6361:20066674.

Cao, Zhen, Felix A. Aharonian, Qi An, L.X. Axikegu, et al. (2021). "Ultrahigh-energy photons up to 1.4 petaelectronvolts from 12 gamma-ray Galactic sources". In: *Nature* 594.7861, pp. 33–36. DOI: 10.1038/s41586-021-03498-z.

Collaboration, Milagro (2004). *Search for very high energy gamma-rays from WIMP annihilations near the Sun with the Milagro Detector*. Also published in Phys. Rev. D 70, 083516 (2004), doi:10.1103/PhysRevD.70.083516. DOI: 10.48550/arXiv.astro-ph/0405291. arXiv: astro-ph/0405291.

Collaboration, The HAWC, A. Albert, et al. (2020a). "3HWC: The Third HAWC Catalog of Very-high-energy Gamma-Ray Sources". In: *The Astrophysical Journal* 905, p. 76. DOI: 10.3847/1538-4357/abc2d8.

— (2020b). "HAWC J2227+610 and Its Association with G106.3+2.7, a New Potential Galactic PeVatron". In: *Astrophysical Journal Letters* 896, pp. L29–L38. DOI: 10.3847/2041-8213/ab96cc.

— (2021). "A Survey of Active Galaxies at TeV Photon Energies with the HAWC Gamma-Ray Observatory". In: *The Astrophysical Journal* 907. DOI: 10.3847/1538-4357/abca9a.

Collaboration, The HAWC, A. U. Albert, et al. (2022). "Constraints on the Very High Energy Gamma-Ray Emission from Short GRBs with HAWC". In: *The Astrophysical Journal* 936.2, p. 126. DOI: 10.3847/1538-4357/ac880e.

De Angelis, A., V. Tatischeff, I. A. Grenier, J. McEnery, et al. (2018). "The e-ASTROGAM mission". In: *Journal of High Energy Astrophysics* 19, pp. 1–106. DOI: 10.1016/j.jheap.2018.07.001.

Di Sciascio, Giuseppe (Apr. 2019). *Ground-based Gamma-Ray Astronomy: an Introduction*. https://arxiv.org/abs/1904.06218. arXiv:1904.06218 [astro-ph.IM].

Dubenskaya, Y. Y., A. P. Kryukov, A. P. Demichev, et al. (2023). "Generating Synthetic Images of Gamma-Ray Events for Imaging Atmospheric Cherenkov Telescopes Using Conditional Generative Adversarial Networks". In: *Moscow University Physics Bulletin* 78.Suppl 1, S64–S70. DOI: 10.3103/S0027134923070056. URL: https://doi.org/10.3103/S0027134923070056.

Errando, Manel and Takayuki Saito (2024). *How to detect gamma-rays from ground: an introduction to the detection concepts*. Submitted 9 Jan 2024. arXiv: 2401.04460v1 [astro-ph.HE]. URL: https://arxiv.org/abs/2401.04460v1.

Fermi, Enrico (1949). "On the Origin of the Cosmic Radiation". In: *Physical Review* 75, pp. 1169–1174.

Fichtel, C. E., R. C. Hartman, D. A. Kniffen, D. J. Thompson, et al. (1975). "High-energy gamma-ray results from the second Small Astronomy Satellite". In: *The Astrophysical Journal* 198, pp. 163–182. DOI: 10.1086/153592.

Funk, Stefan (2015). "Ground- and Space-Based Gamma-Ray Astronomy". In: *Annual Review of Nuclear and Particle Science* 65.1, pp. 245–277. DOI: 10.1146/annurev-nucl-102014-022036. URL: http://dx.doi.org/10.1146/annurev-nucl-102014-022036.

Hess, Victor F. (1912). "Über Beobachtungen der durchdringenden Strahlung bei sieben Freiballonfahrten". In: *Physikalische Zeitschrift* 13.

H.E.S.S. Collaboration (2003). *About H.E.S.S.* https://www.mpi-hd.mpg.de/HESS/pages/about/. Accessed: 2025-06-04.

— (2012). *H.E.S.S. Analysis with HAP: Energy and Angular Reconstruction*. Tech. rep. Internal Analysis Document. Max-Planck-Institut für Kernphysik.

— (2016). "Acceleration of petaelectronvolt protons in the Galactic Centre". In: *Nature* 531, pp. 476–479. DOI: 10.1038/nature17147. URL: https://doi.org/10.1038/nature17147.

— (2018a). *H.E.S.S. A&A Special Issue 2018*. https://www.mpi-hd.mpg.de/hfm/HESS/pages/press/2018/AA-Special-Issue/. Accessed: 2025-06-22.

— (2018b). "The gamma-ray spectrum of the core of Centaurus A as observed with H.E.S.S. and Fermi-LAT". In: *Astronomy & Astrophysics* 619, A71. DOI: 10.1051/0004-6361/201833202. arXiv: 1807.07375 [astro-ph.HE].

Hillas, A. M. (1985). "Cherenkov light images of EAS produced by primary gamma". In: *Proceedings of the 19th International Cosmic Ray Conference*. Vol. 3, pp. 445–448.

Hinton, Jim and Edna Ruiz-Velasco (Feb. 2020). "Multi-messenger astronomy with very-high-energy gamma-ray observations". In: *Journal of Physics: Conference Series* 1468, p. 012096. DOI: 10.1088/1742-6596/1468/1/012096.

Hofman, W. (2012). *The H.E.S.S. Telescopes*. https://www.mpi-hd.mpg.de/hfm/HESS/pages/about/telescopes/. Accessed: 2025-06-04.

Kraushaar, W. L., G. W. Clark, G. P. Garmire, and R. Borken (1965). "High-energy cosmic gamma-ray observations from a balloon". In: *Astrophysical Journal* 141, p. 845. DOI: 10.1086/148186.

Longair, Malcolm S. (2011). *High Energy Astrophysics*. 3rd. Cambridge, UK: Cambridge University Press. ISBN: 9780521756181.

McDonald, Frank B. and Vladimir S. Ptuskin (2001). "Galactic cosmic rays". In: *The Century of Space Science*. Ed. by Johan A. M. Bleeker, Johannes Geiss, and Martin C. E. Huber. Dordrecht: Springer Netherlands, pp. 677–697. ISBN: 978-94-010-0320-9. DOI: 10.1007/978-94-010-0320-9_29. URL: https://doi.org/10.1007/978-94-010-0320-9_29.

Millikan, R. A. and G. H. Cameron (1928). "The Origin of the Cosmic Rays". In: *Physical Review* 32.4, pp. 533–557.

Mirzoyan, R. (2019). "First time detection of a GRB at sub-TeV energies; MAGIC detects the GRB 190114C". In: *The Astronomer's Telegram* 12390. https://www.astronomerstelegram.org/?read=12390.

Murthy, P. V. Ramana and A. W. Wolfendale (1993). *Gamma-Ray Astronomy*. 2nd. Cambridge Astrophysics. Cambridge, UK: Cambridge University Press, p. 2. ISBN: 0-521-42081-4. DOI: 10.1017/CBO9780511564840.

Piel, Q. (2019). "GRB observations with H.E.S.S." In: *36th International Cosmic Ray Conference (ICRC2019)*. PoS(ICRC2019) 686.

Prandini, Elisa, Konstantinos Dialektopoulos, and Jelena Striškovic (2023). "Gamma rays: propagation and detection". In: *arXiv preprint arXiv:2211.17021*. Version 2, submitted on 10 Feb 2023, pp. 11–12. arXiv: 2211.17021 [astro-ph.HE].

Schönfelder, V., H. Aarts, K. Bennett, H. de Boer, et al. (1993). "Instrument description and performance of the imaging Gamma-Ray telescope COMPTEL aboard the Compton Gamma-Ray Observatory". In: *The Astrophysical Journal Supplement Series* 86, pp. 657–692. DOI: 10.1086/191794.

Sinnis, Gus (2009). "Air shower detectors in gamma-ray astronomy". In: *New Journal of Physics* 11.5, p. 055007. DOI: 10.1088/1367-2630/11/5/055007.

Steppa, Constantin (Jan. 2022). "Modelling the galactic population of very-high-energy gamma-ray sources". PhD thesis. universität potsdam. DOI: 10.25932/publishup-54947.

SWGO Collaboration (2023). *Southern Wide-field Gamma-ray Observatory*. https://www.swgo.org/SWGOWiki/doku.php?id=start. Accessed: [10.06.2025].

Thompson, D. J., D. L. Bertsch, C. E. Fichtel, R. C. Hartman, et al. (1993). "Calibration of the Energetic Gamma-Ray Experiment Telescope (EGRET) for the Compton Gamma-Ray Observatory". In: *The Astrophysical Journal Supplement Series* 86, pp. 629–656. DOI: 10.1086/191793.

Vernetto, S. (2012). "Gamma ray sources observation with the ARGO-YBJ detector". In: *Nuclear Instruments and Methods in Physics Research Section A: Accelerators, Spectrometers, Detectors and Associated Equipment* 692. 3rd Roma International Conference on Astroparticle Physics, pp. 34–40. ISSN: 0168-9002. DOI: https://doi.org/10.1016/j.nima.2012.01.041. URL: https://www.sciencedirect.com/science/article/pii/S0168900212000812.

Völk, Heinrich J. and Konrad Bernlöhr (2009). "Imaging Very High Energy Gamma-Ray Telescopes". In: *Experimental Astronomy* 25.1–3, pp. 173–191. DOI: 10.1007/s10686-009-9151-z.

Weekes, T. C., M. F. Cawley, D. J. Fegan, B. Giebels, et al. (1989). "Observation of TeV gamma rays from the Crab nebula using the atmospheric Cherenkov imaging technique". In: *The Astrophysical Journal* 342. DOI: 10.1086/167599.

Acknowledgements

Finally I would like to thank everyone who has been supportive towards me during this thesis work. Special thanks to:

- Prof. Dr. Stefan Funk for allowing me to work on this very interesting topic and for providing very helpful feedback throughout this thesis,
- Dr. Rodrigo Guedes Lang for patiently explaining and clearing all my queries, providing valuable advice and also for proofreading this paper,
- Tim Unbehaun for his support and helping with improving the asymmetrical Gaussian fitting,
- My family and friends for always supporting me.

Declaration of Originality

I, Geethika Konduru, student registration number: 23221480, hereby confirm that I completed the submitted work independently and without the unauthorized assistance of third parties and without the use of undisclosed and, in particular, unauthorized aids. This work has not been previously submitted in its current form or in a similar form to any other examination authorities and has not been accepted as part of an examination by any other examination authority.

Where the wording has been taken from other people's work or ideas, this has been properly acknowledged and referenced. This also applies to drawings, sketches, diagrams and sources from the Internet.

In particular, I am aware that the use of artificial intelligence is forbidden unless its use an aid has been expressly permitted by the examiner. This applies in particular to chatbots (especially ChatGPT) and such programs in general that can complete the tasks of the examination or parts thereof on my behalf.

Any infringements of the above rules constitute fraud or attempted fraud and shall lead to the examination being graded "fail" ("nicht bestanden").

Erlangen, 24.06.25 Geethika Konduru